

Cogging Torque Analysis in Permanent Magnet Machines

Dwaipayan Barman

A Thesis

In the Department

of

Electrical and Computer Engineering

Presented in Partial Fulfillment of the Requirements

For the Degree of

Doctor of Philosophy (Electrical and Computer Engineering) at

Concordia University,

Montréal, Québec, Canada

September 2021

© Dwaipayan Barman, 2021

**CONCORDIA UNIVERSITY
SCHOOL OF GRADUATE STUDIES**

This is to certify that the thesis prepared

By: _____

Entitled: _____

and submitted in partial fulfillment of the requirements for the degree of

Doctor Of Philosophy

complies with the regulations of the University and meets the accepted standards with respect to originality and quality.

Signed by the final examining committee:

	Chair
	External Examiner
	External to Program
	Examiner
	Examiner
	Thesis Supervisor (s)

Approved by _____
Chair of Department or Graduate Program Director

Date of Defence _____
Dean,

Abstract

Cogging Torque Analysis in Permanent Magnet Machines

Dwaipayan Barman, PhD

Concordia University, 2021

This work analyzes cogging torque in special electrical permanent magnet (PM) machines. Cogging torque is the no load reluctance torque. Cogging torque arises due to the magnetic attraction between the slotted stator and permanent magnet at no load. Cogging torque causes acoustic noise and vibration in PM machines. Therefore, it is important to analyze the cogging torque in permanent magnet machines.

The cogging torque is analyzed in a variable flux interior permanent magnet synchronous machine (VF IPMSM). Cogging is computed at different magnetization levels. It is observed that cogging torque is proportional to the magnetic flux density. The effect of optimum skewing angles to minimize the cogging torque is analytically calculated and verified by Finite Element Analysis (FEA). The effect of skewing on back EMF and torque ripple is also investigated in detail. Effect of skewing on the magnetization and demagnetization levels is also analyzed.

One of the major problems of variable flux machines (VFMs) is that PMs are susceptible to unintentional demagnetization by armature reaction. Therefore, a rare earth magnet can be added in series with the Alnico magnet to avoid unintentional demagnetization. But cogging torque is higher in the series hybrid variable flux machine (SVFM). This work computes cogging torque in the SVFM using a lumped magnetic circuit model.

Due to the growing demand for rare-earth magnets and the high variation in its price, the current trend in the research focuses on the design of alternative electric machines technologies that either do not use rare-earth magnets or reduces the required magnet volume. This work computes cogging torque in an asymmetrical interior permanent magnet machine where magnet volume is reduced by 30% to achieve the desired performance.

This research work also investigates the performance of axial flux machines and computes cogging torque with different soft magnetic composite materials.

This dissertation has been prepared using the publication option and is composed of following papers.

Paper I: Effect of Skewing in a Variable Flux Interior Permanent Magnet Synchronous Machine. (D. Barman and P. Pillay, "Effect of Skewing in a Variable Flux Interior Permanent Magnet Synchronous Machine," in *IEEE Transactions on Industry Applications*, vol. 56, no. 6, pp. 6399-6410, Nov.-Dec. 2020)

Paper II: Cogging Torque Analysis in a Series Hybrid Variable flux machines using Lumped Magnetic Circuits. (Accepted in IEEE conference ECCE 2021 and prepared for IEEE Transactions in Industry Applications)

Paper III: Cogging Torque Analysis in an Asymmetrical Interior Permanent Magnet synchronous machine using Lumped Parameter Technique. (Submitted in IEEE Transactions on Magnetics)

Paper IV: Selection of Soft Magnet Composite Material for Electrical Machines using 3D FEA Simulations. (Accepted in IEEE conference ECCE 2021)

ACKNOWLEDGMENTS

I would like to thank Dr. Pragasen Pillay for giving me the opportunity to work in his research group. I would like to acknowledge the financial and technical support they have given to me during my doctoral studies. I would also like to thank, Dr. Chunyan Lai, Dr. Luiz A C Lopes, Dr. Hua Ge for being my committee members and for their valuable inputs. I would like to thank my lab-mates and friends in Concordia University, Montreal, for providing help and support during the course of my doctoral studies at Electrical and Computer Engineering department.

Finally, I would like to thank my parents for making me what I am today. A little time of my PhD that I had with my father was the best. I would like to thank my mother and my sister for always being there helping and supporting me emotionally when I was disappointed during my whole PhD time. My special thanks go to Dr. Mathews and Mr. Tamanwe Payarou, Bigyan Basnet in Concordia University, for their valuable supports during the experiments.

These research works are done as part of NSERC/Hydro-Québec Senior Industrial Research Chair entitled “*Design and Performance of Special Electrical Machines*” held by Professor Pragasen Pillay at Concordia University. The authors acknowledge the support of the Natural Sciences & Engineering Research Council of Canada and Concordia University. The authors also acknowledge the support of cogging torque measurement from Mr. Anant Singh and Dr. Tomy Sebastian from Halla Mechatronics

Chapter 1	1
1 Introduction	1
1.1 Review on Variable Flux Machine	1
1.2 Review on Series Hybrid Variable Flux Machine	3
1.3 Review on Asymmetrical IPM machine	5
1.4 Review on Axial Flux machine	7
2. Motivation	7
3. Organization of the Thesis	9
Chapter 2: Effect of Skewing in a Variable Flux Interior Permanent Magnet Synchronous Machine	10
2.1 INTRODUCTION	11
2.2 CHARACTERIZATION OF THE VARIABLE FLUX MACHINE	13
2.3 COGGING TORQUE REDUCTION	15
2.4 EFFECT OF SKEWING ON BACK EMF	20
2.5 TORQUE RIPPLE SUPPRESSION	23
2.5.A Torque Ripple Factor With 100% Magnetization	24
2.5.B Torque Ripple Factor With 75% Magnetization	26
2.5.C Torque Ripple Factor With 50% Magnetization	27
2.6 DEMAGNETIZATION OF PMS	29
2.6.A Demagnetization of the unskewed PM-pole	29
2.6.B Demagnetization of the 3-step skewed PM-pole	31
2.7 MAGNETIZATION OF PMS	33
2.7.A Magnetization of the unskewed PM-pole	33
2.7.B Magnetization of the 3-step skewed PM-pole	34
2.8 CONCLUSIONS	35
Chapter 3: Cogging Torque Analysis in a Series Hybrid Variable Flux Machine using Lumped Magnetic Circuits	37
3.1 INTRODUCTION	38
3.2 LUMPED MAGNETIC CIRCUIT OF THE SVFM	40
3.3 COGGING TORQUE ANALYSIS	47
3.4 FOURIER COEFFICIENTS	49
3.4.A Determination of G_{anNL}	49
3.4.B Determination of B_{anNL}	51
3.5 EXPERRIMENTAL SETUP	52
3.6 COMPUTATION OF COGGING TORQUE	52
3.7 EFFECT OF COGGING TORQUE	53
3.7.A Back EMF	53
3.7.B Electromagnetic torque	54
3.8 CONCLUSION	55
Chapter 4: Cogging Torque Computation in an Asymmetrical Interior Permanent Magnet Machine Using Lumped Parameter Technique	57
4.1 INTRODUCTION	58
4.2 CHARACTERISTICS OF THE IPM MACHINE	60
4.3 LUMPED MAGNETIC CIRCUIT	61

4.4 DERIVATION OF COGGING TORQUE	65
4.5 FOURIER COEFFICIENTS	67
4.5.A Determination of G_{anNL}	67
4.5.B Determination of B_{anNL} and B_{bnNL}	68
4.6 COMPUTATION OF COGGING TORQUE	69
4.7 COCLUSION	70
Chapter 5: Design of an Axial Flux Machine Using Soft Magnetic Composites	71
5.1 Sizing of Axial Flux Machine	72
5.2 Simulation results	74
5.3 CONCLUSIONS	78
Chapter 6: CONCLUSION and FUTURE WORK	79
REFERENCES	83

List of Figures

Pages No.

Chapter 2: Effect of Skewing in a Variable Flux Interior Permanent Magnet Synchronous Machine	
2.1. 27 slot 6 pole VF IPMSM.	14
2.2. B-H characteristics of AlNiCo9 magnet.	14
2.3. (a) Magnetization and 3(b) demagnetization characteristics of the VF IPMSM.	15
2.4. (a) 2-D sliced rotor of a 3-step skewed VF IPMSM; (b) 2-D sliced rotor of a 5-step skewed VF IPMSM.	16
2.5. Cogging torque of the VF IPMSM at different magnetization levels.	17
2.6. Peak to peak cogging torque of the VF IPMSM versus skewing angle with 3-step and 5-step skewed PM-pole.	18
2.7. Cogging torque of the VF IPMSM with unskewed, 3-step and 5-step skewed PM-pole at 100% magnetization.	18
2.8. Hardware setup for cogging torque measurement of the VF IPMSM.	19
2.9. Simulated and measured cogging torque of the VF IPMSM with unskewed PM-pole at 100% magnetization.	19
2.10. Back EMF comparison at 100% magnetization level.	21
2.11. Harmonic order of back EMF at 100% magnetization level.	21
2.12. Back EMF comparison at 75% magnetization level.	21
2.13. Harmonic order of back EMF at 75% magnetization level.	22
2.14. Back EMF comparison at 50% magnetization level.	22

2.15. Harmonic order of back EMF at 50% magnetization level.	23
2.16. Hardware setup to measure the electromagnetic torque of the VF IPMSM at different magnetization levels	24
2.17. Torque of the VF IPMSM without skewed and with 3-step, 5-step skewed PM-pole for 100% magnetization and skewing angle of $20/3^\circ$	25
2.18. Harmonic order of torque at 100% magnetization level.	25
2.19. Torque of the VF IPMSM without skewed and with 3-step, 5-step skewed PM-pole for 75% magnetization and skewing angle of $20/3^\circ$.	26
2.20. Harmonic order of torque at 75% magnetization level	26
2.21. Torque of the VF IPMSM without skewed and with 3-step, 5-step skewed PM for 50% magnetization and skewing angle of $20/3^\circ$	28
2.22. Harmonic order of torque at 50% magnetization level.	28
2.23. The VF IPMSM with six probes along the length of PM.	29
2.24. Demagnetizing d-axis current pulse to demagnetize the PMs of the VF IPMSM.	30
2.25. Magnet flux density of the VF IPMSM before and after applying the demagnetizing current pulse.	30
2.26. Magnet flux distribution of the unskewed PM-pole.	30
2.27. Magnet flux density of 1st step of 3-step skewed PM-pole before and after applying demagnetizing current pulse for skewing angle (a) $20/3^\circ$ (b) $40/3^\circ$.	31
2.28. Magnet flux density of 2nd step of 3-step skewed PM-pole before and after applying demagnetizing current pulse for skewing angle (a) $20/3^\circ$ (b) $40/3^\circ$.	32
2.29. Magnet flux density of 3rd step of 3-step skewed PM-pole before and after applying demagnetizing current pulse for skewing angle (a) $20/3^\circ$ (b) $40/3^\circ$.	33
2.30. Pulse 1 represents demagnetizing d-axis current, and pulse 2 represents magnetizing d-axis current.	34
2.31. Magnet flux density of the VF IPMSM after applying the magnetizing current pulse.	34
2.32. Magnet flux density of 1st step of 3-step skewed PM-pole before and after applying magnetizing current pulse for skewing angle $20/3^\circ$	34
2.33. Magnet flux density of 2nd step of 3-step skewed PM-pole before and after applying magnetizing current pulse for skewing angle $20/3^\circ$.	35
2.34. Magnet flux density of 3rd step of 3-step skewed PM-pole before and after applying magnetizing current pulse for skewing angle $20/3^\circ$.	35
Chapter 3: Cogging Torque Analysis in a Series Hybrid Variable Flux Machine using Lumped Magnetic Circuits	37
3.1. Flux lines in the SVFM.	41

3.2. Dimensions of the slot-less 6-pole SVFM.	41
3.3. Lumped magnetic circuit of the SVFM.	42
3.4. Simplified lumped magnetic circuit of the SVFM.	42
3.5. Flux density comparison at 100% magnetization level.	46
3.6. Flux density comparison at 75% magnetization level.	46
3.7. Flux density comparison at 50% magnetization level.	46
3.8. 1/6th of the 36-slot 6-pole SVFM.	48
3.9. Magnetic flux density vector plot of the 36-slot 6-pole SVFM at 100% magnetization and no load.	48
3.10. Simplified model: (a) a slot and (b) corresponding relative air gap permeance.	50
3.11. Ideal distribution of air-gap flux density for one PM-pole.	51
3.12. Hardware setup to measure cogging torque.	52
3.13. Cogging torque comparison at 100% magnetization of AlNiCo9 magnet.	53
3.14. Cogging torque comparison at 50% magnetization of AlNiCo9 magnet.	53
3.15. Back EMF at different magnetization levels.	54
3.16. Torque at different magnetization levels.	55
Chapter 4: Cogging Torque Computation in an Asymmetrical Interior Permanent Magnet Machine Using Lumped Parameter Technique	57
4.1. Characteristics of the asymmetrical IPM machine [2].	60
4.2. 4-pole IPM including flux lines.	61
4.3. Necessary dimensions to develop lumped model.	61
4.4. B-H characteristics of M36G29 steel.	63
4.5. Lumped magnetic model of the asymmetrical IPM machine.	63
4.6. Comparison of air gap flux density.	64
4.7. A simplest slot.	68

4.8. Relative air gap permeance function.	68
4.9. Ideal flux distribution.	68
4.10. Hardware setup.	68
4.11. Cogging torque.	69
Chapter 5: Design of an Axial Flux Machine Using Soft Magnetic Composites	71
5.1 Major dimensions	72
5.2. Full model of the 12-slot 14-pole 15 kW DSSR AFPM machine	75
5.3. Quarter model of the DSSR AFPM machine	75
5.4. Cogging torque of the DSSR AFPM machine with materials A, B, C.	76
5.5. Back EMF of the DSSR AFPM machine with materials A, B, C.	76
5.6. Torque of the DSSR AFPM machine with materials A, B, C at rated current 50.2	76
5.7. Loss comparison of the 15 kW DSSR AFPM machine with A, B, C materials.	77
5.8. Efficiency comparison with 3 different materials	78

List of TABLE

Pages No.

Chapter 2: Effect of Skewing in a Variable Flux Interior Permanent Magnet Synchronous Machine	
Table 2.1. SPECIFICATIONS OF THE 27 SLOT 6 POLE VF IPMSM	13
Table 2.2. TORQUE RIPPLE OF THE VF IPMSM FOR 100% MAGNETIZATION	25
Table 2.3. TORQUE RIPPLE OF THE VF IPMSM FOR 75% MAGNETIZATION	27
Table 2.4. TORQUE RIPPLE OF THE VF IPMSM FOR 50% MAGNETIZATION	28
Chapter 3: Cogging Torque Analysis in a Series Hybrid Variable Flux Machine using Lumped Magnetic Circuits	
Table 3.1. MACHINE DESIGN PARAMETERS	45
Table 3.2. AIR GAP FLUX DENSITY	46

Table 3.3. SPECIFICATION OF THE 36-SLOT 6-POLE SVFM	49
Table 3.4. EFFECT OF COGGING TORQUE on Back EMF	54
Table 3.5. EFFECT OF COGGING TORQUE ON TORQUE	55
Chapter 4: Cogging Torque Computation in an Asymmetrical Interior Permanent Magnet Machine Using Lumped Parameter Technique	
Table 4.1. NECESSARY DIMENSIONS AND PARAMETERS	63
Table 4.2. COMPARISON BETWEEN FEA AND ANALYTICAL	64
Chapter 5: Design of an Axial Flux Machine using Soft Magnetic Composites	
Table 5.1. SPECIFICATIONS OF THE 12 SLOT 14 POLE AFPMSM	74
Table 5.2. DETAIL OF THE 12 SLOT 14 POLE AFPM MACHINE	77

Chapter 1

1. Introduction

This research focuses on cogging torque in special permanent magnet (PM) machines and as well as the scope of axial flux machines for EV applications with different soft magnetic composite (SMC) materials. This research work discusses cogging torque in a variable flux interior permanent magnet synchronous machine (VF IPMSM). But the variable flux machine (VFM) is prone to armature demagnetizing field. Therefore, a rare earth magnet is added in series with the Alnico in the VFM. This is called a series hybrid variable flux machine (SVFM). The cogging torque in a 36-slot 6-pole SVFM is analyzed in detail later.

Electric motors for vehicle applications need a broad speed range with higher torque density and efficiency. Permanent magnet synchronous machines (PMSM) have higher efficiency and higher torque density compared with induction and synchronous reluctance machines. Thus, they are extensively used in vehicle applications. However, due to the growing demand for rare-earth magnets and the high variation in its price, the current trend in the research focuses on the design of alternative electric machines technology that either does not use the rare-earth magnets or reduces the required magnet volume. Therefore, a novel asymmetrical machine is designed where magnet torque is aligned with reluctance torque and thus, torque density is enhanced. Cogging torque of the asymmetrical IPM is analyzed. This research work discusses about the selection of proper soft magnetic materials in axial flux machine for EV applications.

1.1 Review on Variable Flux Machine

Permanent Magnet Synchronous Machines (PMSMs) are highly popular as they provide

high efficiency and high torque density compared to the conventional induction and synchronous machines. The PMSMs can be less efficient above the base speed in the field weakening region due to continuous d-axis current. The variable flux PM machines (VFM) can provide higher efficiency compared to conventional PMSMs in the field weakening region [1]-[2]. A comparison between the PMSMs and the VFMs in terms of the operating point envelopes, efficiency and speed extension were discussed in detail in [1]. The concept of the VFM was explained well in [2]-[4]. PMSMs can operate at high flux density and torque density if the armature reaction is neglected. In [2], a high torque density VFM was designed with tangentially magnetized AlNiCo9 magnets to avoid the armature demagnetization. A design approach for the VFMs based on field intensifying interior PM types and using stator windings to change the magnetization state was studied in [5]. A stator design with higher teeth width was more desirable for reducing the required magnetizing state control current. Different types of series [6]-[8] or parallel [6], [7] hybrid VFMs provided better magnet flux controllability. A spoke type variable flux machine was designed in [9] using Alnico magnets and an analytical approach based on the magnetization current and the torque mean value was proposed and verified using two dimensional (2-D) FEA.

One of the major issues of AlNiCo based PMSMs is the cogging torque and the resulting torque ripple. Cogging torque arises due to the reluctance variation between the slotted stator and the PMs on the rotor. Different techniques to minimize the cogging torque were mentioned in [10], [11], and [14]. The effects of the design parameters such as slot and pole number, pole arc design, skewing angle and slot opening on the cogging torque were studied. In [12], the cogging torque in an IPMSM was reduced using a step skewed rotor. A

vector diagram was used to analyze a 3-step skewed rotor followed by a 2-D FEA validation. The cogging torque was reduced by the pole arc design and PM shifting in [13].

The reasons for the torque ripple in PMSMs were analyzed in [15], [16]. Torque ripple minimization techniques in PMSMs were examined in detail in [15]-[19]. In [20], the effects of electrical, magnetic and geometrical parameters such as load, magnetization level of magnets, tooth and yoke width and magnet dimensions on both average torque and torque ripple of a VF IPMSM were studied. The torque ripple value was reduced by 35% in [20]. In [21], a vector-controlled drive was used to measure the torque of a VFM, and the torque ripple was found for different levels of magnetizations. The results showed that the torque ripple was higher for lower levels of magnetization [21], [22]. Also, the back EMF and the torque angle characterization of a VF IPMSM were analyzed in [23]-[25].

Another important issue in the VFM is the application of the proper current pulse required to magnetize or demagnetize a step skewed PM-pole. The required demagnetizing current was applied and the demagnetization of each step of the step skewed PM-pole was investigated in [14]. The magnetization and demagnetization characteristics of the VF IPMSM were examined in detail in [25]. A VF IPMSM with lower magnetizing current was mentioned in [26].

1.2 Review on Series Hybrid Variable Flux Machine (SVFM)

The conventional permanent magnet synchronous machines (PMSMs) with rare earth magnets have challenges in wide speed region due to requirement of a continuous d-axis demagnetizing current in the field weakening operation [29]. The demagnetizing d-axis current causes additional copper loss of the rare earth PMSMs. In order to enhance the wide

speed region, a variable flux machine (VFM) using lower coercive force magnet AlNiCo9 was proposed [4], [6], [30] - [32] where the d-axis demagnetizing current was reduced significantly. However, the lower coercive force AlNiCo9 magnet is prone to armature demagnetization field. On the other hand, in a 36-slot 6-pole SVFM in [33], the higher coercive force N48SH magnet raised the operating point of the lower coercive force AlNiCo9 magnet, thus improving the machine performance with a stable field weakening operation.

One of the major problems of the 36-slot 6-pole SVFM is cogging torque. Cogging torque is the no load reluctance torque due to the magnetic attraction between the permanent magnets (PMs) and slotted stator at no load. The cogging torque causes torque ripple and does not contribute to the net effective torque [15]. Therefore, it is very essential to calculate the value of the cogging torque in the 36-slot 6 pole SVFM. The analytical models for predicting the cogging torque in surface-mounted permanent-magnet machines (SPMSMs), viz., lateral force, complex permeance, and exact subdomain models, together with a subdomain model based on a single slot/pole were analyzed in [34]. A simple analytical technique was proposed to synthesize the cogging-torque waveform of a permanent magnet brushless machine from the cogging torque, which is associated with a single stator slot [35]. A method for predicting the cogging torque in radial field permanent magnet brushless motors, based on the analytical calculation of the air gap field distribution and the net lateral force acting on the stator teeth, was developed and validated [36].

The cogging torque of the 36-slot, 6-pole SVFM is computed using a Fourier series expansion of the air gap flux density in an equivalent slot-less machine and the relative air gap permeance function [11], [18]. The air gap flux density is calculated using a lumped

magnetic circuit model in this article. Although the FEA can accurately calculate the flux density distribution in the air gap, it often requires a higher computation time to verify a design. Therefore, a lumped magnetic circuit model [37]-[40] can be used to reduce the computation time with sufficient accuracy to calculate the air gap flux density. A simple lumped magnetic circuit model for interior permanent-magnet (IPM) machines with multi-segment and multilayer permanent magnets was presented in [41]. The open-circuit air-gap field distribution, average air gap flux density, and leakage fluxes were derived analytically. The cogging torque waveform of the interior permanent magnet (IPM) machine was predicted using only an analytical model based on the proposed virtual permanent magnet (PM) concept, IPM was considered as surface PM having zero height and unit relative permeability [42]. A new analytical model for estimating the cogging torque in a multi flux-barrier interior permanent magnet machine (IPM) based on a lumped magnetic circuit considered the saturated bridge in the rotor's iron core [43].

1.3 Review on Asymmetrical IPM machine

Electric motors for vehicle applications require wide speed range with higher torque density and efficiency [48]. Permanent magnet synchronous machines (PMSM) can operate with high torque density and efficiency compared with similar induction machines. But the price of the rare earth magnets is higher. Therefore, current research looks for electrical machine technology that avoids rare earth materials or achieve the similar desired performance with lower magnet volume.

This article develops the lumped magnetic circuit of a novel asymmetrical IPM machine where the magnet torque is aligned with reluctance torque to enhance the torque density with reduced magnet volume. A flux barrier is introduced so that the magnet and reluctance axes move from their conventional positions. The peak value of magnet torque is then aligned with peak value of the reluctance torque. Thus, higher torque density in the asymmetrical IPM machine was achieved with lower magnet volume [49].

One of the major problems of the asymmetrical IPM machine is higher cogging torque and torque ripple [19],[50],[51]. The higher cogging torque in the asymmetrical IPM machine can create acoustic noise and vibration [52]. Therefore, it is crucial to know the value of the cogging torque in the asymmetrical IPM machine. The cogging torque in the asymmetrical IPM machine occurs due to the magnetic attraction between the permanent magnets (PMs) and slotted stator at no load. This cogging torque can create torque ripple at rated load operation [18]. Therefore, learning and minimizing the value the cogging torque in the asymmetrical IPM machine is highly important.

The cogging torque in the asymmetrical IPM machine can be computed based on a Fourier series of the asymmetrical flux distribution in the air gap in an equivalent slot-less PM machine and the relative air gap permeance function [13]. Although finite-element analysis (FEA) can precisely obtain the flux density distribution, it can create computational burden and still often used only for design validation. Therefore, a lumped magnetic circuit model can be used for simplicity and sufficient accuracy [18], [37]–[40], [53]–[55]. The asymmetrical flux distribution in the 36-slot 4-pole IPM machine can be computed using an equivalent lumped magnetic circuit model derived based on the FEA results [41].

Lumped magnetic circuits are particularly applicable for IPM machines due to extremely saturated rotor bridges and intricate rotor configurations. The rotor bridges could be modeled as constant flux leakage sources with preset values [54], [55] or nonlinear permeance elements using iterative process [18], [38], [53]. Although the assumption in [38]–[40] might be incorrect since the saturation level of the rotor iron bridge could be changed under different loading conditions, it was reasonably acceptable for estimation as it could result in significant simplification.

1.4 Review on Axial Flux machine

This work investigates the scope of soft magnetic composite materials in a dual stator single rotor axial flux machine [61] for EV applications [62]. A dual stator single rotor (DSSR) axial flux machine is designed using the formulas in [63]. The axial flux machine is simulated with three different soft magnetic composite materials (SMC) of Somaloy. One of the three materials have lower conductivity (70 S/m), One has medium conductivity (600 S/m) and one with higher conductivity (6000 S/m). Then, proper soft magnetic composite material is chosen for EV applications with higher efficiency.

2. Motivation.

1. The motivation of this work is to investigate the effect of skewing on the cogging torque and the torque ripple in a 3 phase 27 slot 6 pole VF IPMSM for minimum optimum skewing angle. The optimum skewing angle to minimize the cogging torque is found analytically and verified by using FEA. A proper current pulse is required to magnetize or demagnetize each step of the step skewed PM-pole. The magnetizing or demagnetizing current pulse is applied to the step skewed PM-pole and the magnetization level of each step

in a PM-pole is investigated. The effect of the step skewed PM-pole on the cogging torque, back EMF, and torque ripple in the 27 slot 6 pole VF IPMSM is studied with different magnetization levels.

2. This work calculates the open circuit air gap flux density using a lumped magnetic circuit in the slot-less 6-pole SVFM at different magnetization levels of the AlNiCo9 magnet. The lumped magnetic circuit is developed based on the magnetic flux lines obtained in the FEA. The computed air gap flux density in the slot-less SVFM is compared to the FEA results at 100%, 75%, and 50% magnetization levels of the AlNiCo9 magnet. Thus, the magnetic circuit model is validated. The cogging torque is computed based on the Fourier series of the air gap flux density in an equivalent slot-less machine and the relative air gap permeance function and compared to the FEA results at different magnetization levels of the AlNiCo9 magnet.

3. This work presents improved lumped magnetic circuit models for analytically predicting the open-circuit air-gap flux density distributions in a 36-slot 4-pole asymmetrical IPM machine. Based on the analysis of flux lines obtained by FEA, simplified lumped magnetic circuits are obtained and Kirchhoff's law is used for deriving the analytical expressions of the leakage fluxes [41].

The cogging torque of the asymmetrical 36-slot 4-pole IMP machine is derived based on the available information of cogging torque available in the literature [11], [56]-[58]. Finally, the cogging torque in the asymmetrical IPM machine is computed using the open circuit air gap flux density in an equivalent slot-less machine and unit relative air gap permeance function. The computed cogging torque is compared to the FEA and experimental results.

4. A dual stator single rotor (DSSR) axial flux machine is designed for a 15 kW operation. The DSSR axial flux machine is simulated with three different soft magnetic composite materials. The soft magnetic composite material that provides higher efficiency is selected for the stator core material.

3. Organization of the Thesis

This thesis consists of six chapters. Chapter 1 presents about a general overview and introduction of the thesis. Chapter 2 analyses cogging torque in a variable flux interior permanent magnet synchronous machine. This resulted in the following publication, “D. Barman and P. Pillay, "Effect of Skewing in a Variable Flux Interior Permanent Magnet Synchronous Machine," in *IEEE Transactions on Industry Applications*, vol. 56, no. 6, pp. 6399-6410, Nov.-Dec. 2020. Chapter 3 analyzes cogging torque in a series hybrid variable flux machine using lumped magnetic circuits. This is accepted in the IEEE ECCE conference 2021, “Cogging Torque Analysis in a Series Hybrid Variable flux machines using Lumped Magnetic Circuits” and will be submitted for IEEE Transactions in Industry Applications after presentation in ECCE. Chapter 4 computes cogging torque in an asymmetrical interior permanent magnet machine using lumped magnetic circuits. This has been submitted to the IEEE Transactions on Magnetics,” Cogging Torque Analysis in an Asymmetrical Interior Permanent Magnet synchronous machine using Lumped Parameter Technique”. Chapter 5 discusses the design of a dual stator single rotor axial flux machine with different soft magnetic composite materials. This has been accepted in the IEEE ECCE conference 2021,” Selection of Soft Magnet Composite Material for Electrical Machines using 3D FEA Simulations”. Finally, the thesis is concluded in chapter 6.

Chapter 2

Effect of Skewing in a Variable Flux Interior Permanent Magnet

Synchronous Machine

2.1 INTRODUCTION

Permanent Magnet Synchronous Machines (PMSMs) are highly popular as they provide high efficiency and high torque density compared to the conventional induction and synchronous machines. The PMSMs can be less efficient above the base speed in the field weakening region due to continuous d-axis current. The variable flux PM machines (VFM) can provide higher efficiency compared to conventional PMSMs in the field weakening region [1]-[2]. A comparison between the PMSMs and the VFMs in terms of the operating point envelopes, efficiency and speed extension were discussed in detail in [1]. The concept of the VFM was explained well in [2]-[4]. PMSMs can operate at high flux density and torque density if the armature reaction is neglected. In [2], a high torque density VFM was designed with tangentially magnetized AlNiCo9 magnets to avoid the armature demagnetization. A design approach for the VFMs based on field intensifying interior PM types and using stator windings to change the magnetization state was studied in [5]. A stator design with higher teeth width was more desirable for reducing the required magnetizing state control current. Different types of series [6]-[8] or parallel [6], [7] hybrid VFMs provided better magnet flux controllability. A spoke type variable flux machine was designed in [9] using Alnico magnets and an analytical approach based on the magnetization current and the torque mean value was proposed and verified using two dimensional (2-D) FEA.

One of the major issues of AlNiCo based PMSMs is the cogging torque and the resulting torque ripple. Cogging torque arises due to the reluctance variation between the slotted stator and the PMs on the rotor. Different techniques to minimize the cogging torque were mentioned in [10], [11], and [14]. The effects of the design parameters such as slot and pole number, pole arc design, skewing angle and slot opening on the cogging torque were studied. In [12], the cogging torque in an IPMSM was reduced using a step skewed rotor. A vector

diagram was used to analyze a 3-step skewed rotor followed by a 2-D FEA validation. The cogging torque was reduced by the pole arc design and PM shifting in [13].

The reasons for the torque ripple in PMSMs were analyzed in [15], [16]. Torque ripple minimization techniques in PMSMs were examined in detail in [15]-[19]. In [20], the effects of electrical, magnetic and geometrical parameters such as load, magnetization level of magnets, tooth and yoke width and magnet dimensions on both average torque and torque ripple of a VF IPMSM were studied. The torque ripple value was reduced by 35% in [20]. In [21], a vector-controlled drive was used to measure the torque of a VFM, and the torque ripple was found for different levels of magnetizations. The results showed that the torque ripple was higher for lower levels of magnetization [21], [22]. Also, the back EMF and the torque angle characterization of a VF IPMSM were analyzed in [23]-[25].

Another important issue in the VFM is the application of the proper current pulse required to magnetize or demagnetize a step skewed PM-pole. The required demagnetizing current was applied and the demagnetization of each step of the step skewed PM-pole was investigated in [14]. The magnetization and demagnetization characteristics of the VF IPMSM were examined in detail in [25]. A VF IPMSM with lower magnetizing current was mentioned in [26].

The motivation of this work is to investigate the effect of skewing on the cogging torque and the torque ripple in a 3 phase 27 slot 6 pole VF IPMSM for minimum optimum skewing angle. The optimum skewing angle to minimize the cogging torque is found analytically and verified by using FEA. A proper current pulse is required to magnetize or demagnetize each step of the step skewed PM-pole. The magnetizing or demagnetizing current pulse is applied to the step skewed PM-pole and the magnetization level of each step in a PM-pole is

investigated. Effect of the step skewed PM-pole on the cogging torque, back EMF, and torque ripple in the 27 slot 6 pole VF IPMSM is studied with different magnetization levels.

2.2 CHARACTERIZATION OF THE VARIABLE FLUX MACHINE

The specifications of the 27 slot 6 pole VF IPMSM is given in table 2.1. The conventional PMSMs require continuous negative d-axis current to change the magnetization level whereas the VFMs require a negative d-axis current pulse to change the magnetization level. Therefore, the magnetization level of conventional PMSMs is essentially constant whereas it can change for VF IPMSM. The efficiency of the VF IPMSM can be enhanced in the field weakening region due to the elimination of continuous d-axis current.

Table 2.1: Specifications of the 27 slot 6 pole VF IPMSM

Machine parameters	Machine specifications
Rated power	7.5 hp
DC bus voltage	600 V
Rated current	10 A
Rated speed	1200 rpm
Outer diameter	200 mm
Inner diameter	109 mm
Air gap	0.4 – 0.75 mm
Number of slots	27
Number of pole	6
Stack length	120 mm
PM material	AlNiCo9
Magnet remnant flux density	1.08 T
Steel material	M1929G

The VF IPMSM used in this work is an AlNiCo9 based VFM [2], [21] as shown in Fig. 2.1. The greatest common divisor of the number of slots and poles is 3. Therefore, the VF IPMSM has a magnetic symmetry of mechanical 120 degree as shown in Fig. 2.1. The air gap in the VFM varies gradually from 0.4 mm in the d-axis to 0.75 mm in the q-axis to reduce the total harmonic distortion (THD) in the back EMF in addition to minimizing the magnetizing current. The stator and the rotor core consist of M19 29G steel material. AlNiCo9 is used as a

source of excitation in the rotor due to a lower coercive force. Therefore, the magnetization level of AlNiCo9 based VF IPMSM can be easily changed.

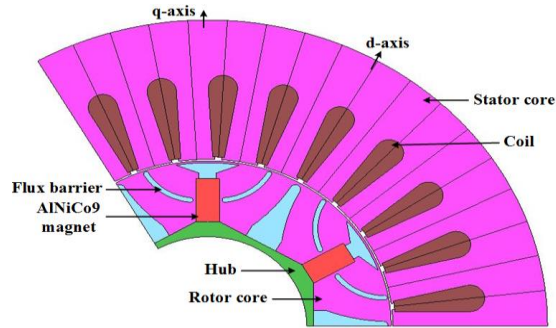


Fig. 2.1. 27 slot 6 pole VF IPMSM.

Fig. 2.2 shows the operating points of the AlNiCo9 magnet under the operation of magnetizing and demagnetizing current field.

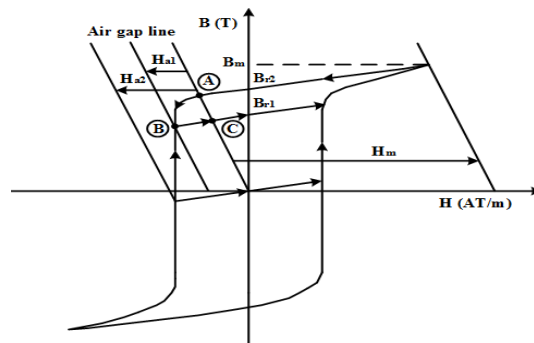


Fig. 2.2 B-H characteristics of AlNiCo9 magnet.

The AlNiCo9 magnet recoils through a different line in the second quadrant when the demagnetizing current field is withdrawn. Similarly, AlNiCo9 magnet recoils through a different line in the first quadrant when the magnetizing current is withdrawn. Thus, the magnetization and demagnetization characteristics of the AlNiCo9 magnet are defined.

The measured and FEA results of the magnetizing and demagnetizing characteristics of the AlNiCo9 magnet are shown in Fig. 2.3(a) and 2.3(b), respectively.

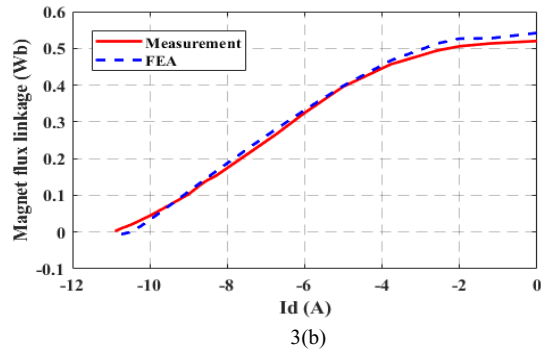
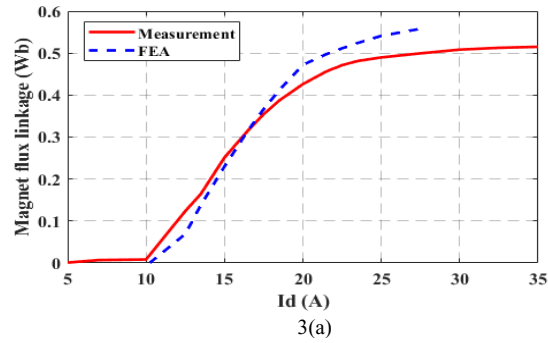


Fig. 2.3. (a) Magnetization and (b) demagnetization characteristics of the VF IPMSM.

In Fig. 2.3, let the initial magnet flux linkage be 0.4 Wb in the FEA curve. Therefore, a d-axis current between -5 A to 18 A will have no effect on the magnet flux linkage. The magnet flux linkage changes when the d-axis current is below -5 A or higher than 18 A. The required magnet flux linkage is controlled by the application of the proper d-axis current pulse based on these magnetization and demagnetization characteristics. This ensures that each magnetization level is not affected for a certain range of d-axis current.

2.3 COGGING TORQUE REDUCTION

Cogging torque is the no-load reluctance torque as the machine rotates. Cogging torque arises due to the magnetic attraction between the PMs and the slotted stator at no-load and contributes to the acoustic noise and vibration if the machine is not properly designed. Cogging torque does not contribute to the net effective torque.

Different cogging torque minimization techniques were already mentioned in [10]-[14]. The cogging torque of the 27 slot 6 pole VF IPMSM at 100% magnetization is simulated using FEA and minimized by skewing the PM-pole for several steps. The optimum skewing angle to minimize the cogging torque is found analytically. The VF IPMSM has a magnetic symmetry of mechanical 120° . Therefore, a mechanical 120° sliced rotor of the VF IPMSM with 3-step and 5-step skewed PM-pole is shown in Fig. 2.4(a) and 2.4(b), respectively.

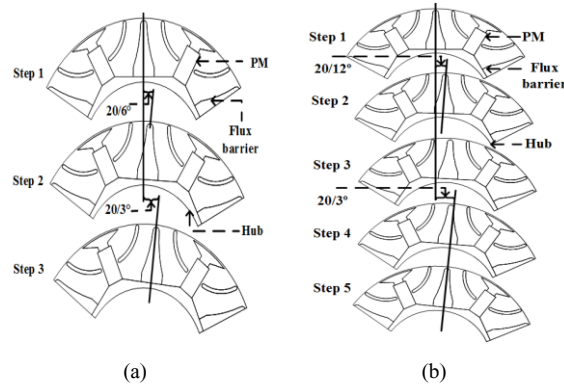


Fig. 2.4. (a) 2-D sliced rotor of a 3-step skewed VF IPMSM; (b) 2-D sliced rotor of a 5-step skewed VF IPMSM.

Cogging torque was derived in [11], [13] by using the Fourier series expansion based on the relative air gap permeance function and the flux density in an equivalent slot-less PMSM. The optimum skewing angles to eliminate the cogging torque were mentioned in [11], [13] and given by equation (2.1).

$$\theta_{skew} = \frac{2k\pi}{N_L} [k = 1, 2, 3, \dots] \quad (2.1)$$

θ_{skew} is optimum skewing angle to eliminate the cogging torque theoretically. N_L is the least common multiple of the number of slots and the number of poles and also the fundamental period of the cogging torque. Effect of skewing on the cogging torque is analyzed with 100% magnetization level. The cogging torque magnitude is higher at 100% magnetization

compared to 75% and 50% magnetization. The cogging torque of the VF IPMSM is shown with different magnetization levels of AlNiCo9 magnet in Fig. 2.5.

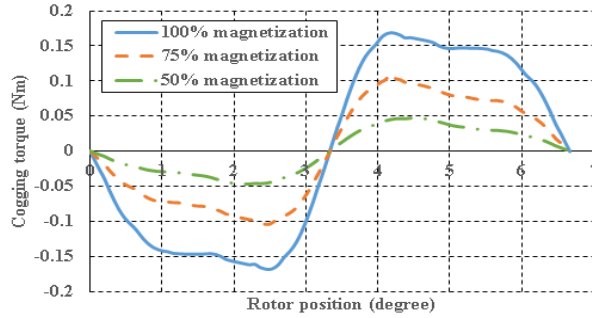


Fig. 2.5. Cogging torque of the VF IPMSM at different magnetization levels.

The optimum skewing angles are independent of the magnetization levels since the period of the cogging torque observed in Fig. 2.5 is same for all the magnetization levels of the AlNiCo9 magnet. The optimum skewing angles calculated by using equation (2.1) to eliminate the cogging torque for the VF IPMSM are $20/3^\circ$, $40/3^\circ$, 20° , etc. A skewing angle of more than one slot pitch reduces the average electromagnetic torque of a machine and makes the manufacturing of the machine more difficult. The slot pitch of the VF IPMSM used is $40/3^\circ$. Therefore, the peak to peak cogging torque of the VF IPMSM at 100% magnetization is varied against skewing angle from 1° to 16° . The peak to peak cogging torque versus skewing angle is shown in Fig. 2.6 for a 3-step and a 5-step skewed PM-pole.

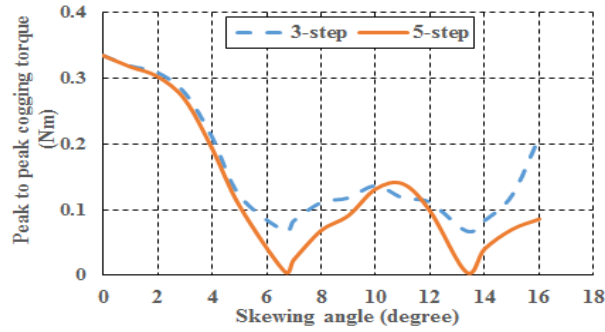


Fig. 2.6. Peak to peak cogging torque of the VF IPMSM versus skewing angle with 3-step and 5-step skewed PM-pole.

Optimum skewing angles obtained by equation (2.1) are verified by the FEA results as shown in Fig. 2.6. The peak to peak cogging torque is minimum at $20/3^\circ$, $40/3^\circ$ in both the 3-step and the 5-step skewed PM-pole. The reduction of the cogging torque is higher at the optimum skewing angles with a 5-step skewed PM-pole compared to the 3-step skewed PM-pole. The cogging torque of the VF IPMSM at 100% magnetization is shown in Fig. 2.7 with unskewed, 3-step and 5-step skewed PM-pole for a skewing angle of $20/3^\circ$. The fundamental period of the cogging torque of the VF IPMSM without skewing is $20/3^\circ$ [14]. The peak to peak cogging torque is reduced by 88% for the 3-step skewed PM-pole and 99% for the 5-step skewed PM-pole compared to the unskewed PM-pole and rotor. Therefore, the cogging torque reduction is higher with the 5-step skewed PM design than the 3-step design.

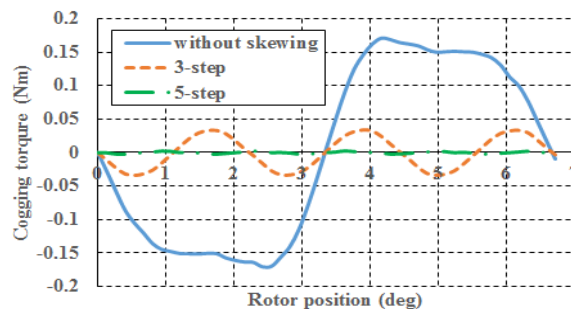


Fig. 2.7. Cogging torque of the VF IPMSM with unskewed, 3-step and 5-step skewed PM-pole at 100%

The value of the peak to peak cogging torque at a skewing angle of $20/3^\circ$ is identical to the skewing angle of $40/3^\circ$ for both the 3-step and the 5-step skewed PM-pole as observed in Fig. 2.6. Cogging torque of the VF IPMSM with unskewed PM-pole at 100% magnetization is measured and compared with the FEA result. The hardware setup for cogging torque measurement is shown in Fig. 2.8. Torque is applied on the shaft of the VF IPMSM with the help of a torque arm and position information is obtained from the position encoder.

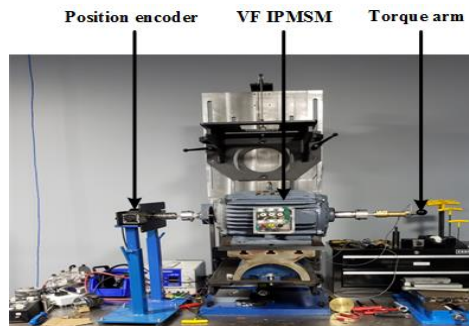


Fig. 2.8. Hardware setup for cogging torque measurement of the VF IPMSM.

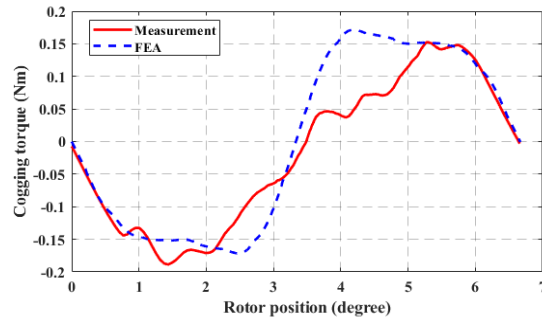


Fig. 2.9. Simulated and measured cogging torque of the VF IPMSM with unskewed PM-pole at 100% magnetization.

Fig. 2.9 shows both simulated and measured cogging torque for the VF IPMSM with unskewed PM-pole for one period. The VFM used has a rotor eccentricity at 100% magnetization level. The eccentricity can be due to the unbalanced magnetic attraction

between the AlNiCo9 magnet and the stator. This can create the difference in the FEA and experimental results of the cogging torque at 100% magnetization level.

2.4 EFFECT OF SKEWING ON BACK EMF

This section analyzes the effect of skewing on the back EMF at different magnetization levels of AlNiCo9 magnet. The major components of harmonics along with the THD of the back EMF is presented for each magnetization level. The minimum optimum skewing angle chosen for the step skewed PM-pole is $20/3^\circ$. The skewing mainly affects the slot harmonics and the space harmonics (5th and 7th) are not significantly affected by skewing. The slot harmonics are given as:

$$h_s = nq \pm 1 (n = 1, 2, 3, \dots) \quad (2.2)$$

Where, h_s represents the slot harmonics and q is the number of slots per pole pair.

The effect of skewing on the back EMF of the VF IPMSM is studied at 100% magnetization level of AlNiCo9 magnet. The FEA and measured results of the back EMF without skewing are shown in Fig. 2.10. The FEA results of the back EMF with 3-step and 5-step skewed PM-pole are also shown in the same figure. The major harmonic components along with the percentage THD for each waveform are given in Fig. 2.11. The fundamental component of the phase back EMF obtained from the FEA without skewed PM-pole is 144.6 V whereas the measured value is 134.4 V.

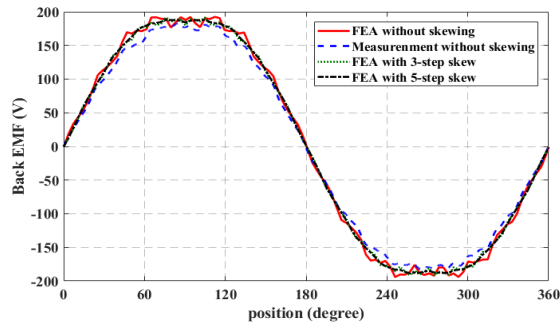


Fig. 2.10. Back EMF comparison at 100% magnetization level.

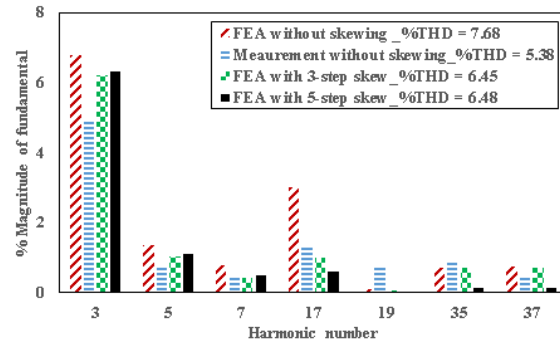


Fig. 2.11. Harmonic order of back EMF at 100% magnetization level.

The FEA and measured back EMF of the VF IPMSM without skewing at 75% magnetization are shown in Fig. 2.12. The FEA results of the back EMF with the 3-step and 5-step skewed PM-pole are also provided in the same figure. The major harmonic components of each back EMF waveform are shown in Fig. 2.13. The fundamental of the phase back EMF obtained from the FEA without skewed PM-pole is 106.7 V whereas the measured value is 100.9 V.

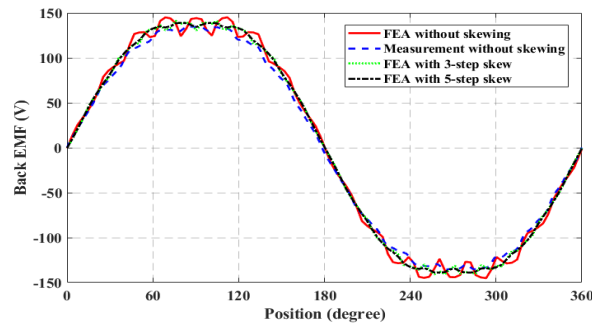


Fig. 2.12. Back EMF comparison at 75% magnetization level.

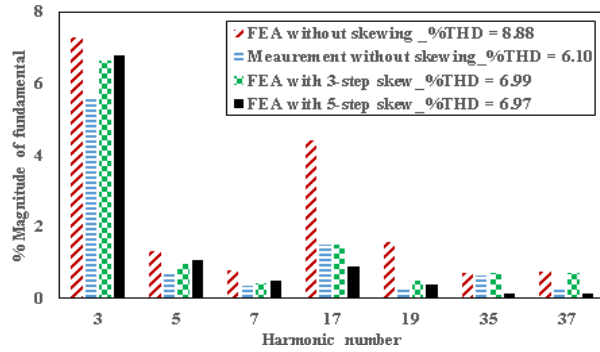


Fig. 2.13. Harmonic order of back EMF at 75% magnetization level.

The FEA and measured back EMF of the VF IPMSM without skewing at 50% magnetization are shown in Fig. 2.14. The FEA results of the back EMF with the 3-step and the 5-step skewed PM-pole are provided in the same figure. The major harmonic orders of each back EMF waveform are provided in Fig. 2.15. The fundamental of the phase back EMF obtained from the FEA without skewed PM-pole is 67.6 Volt where the measured value is 66.2 Volt.

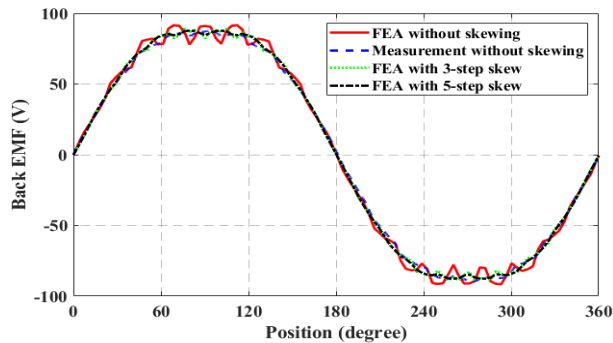


Fig. 2.14. Back EMF comparison at 50% magnetization level.

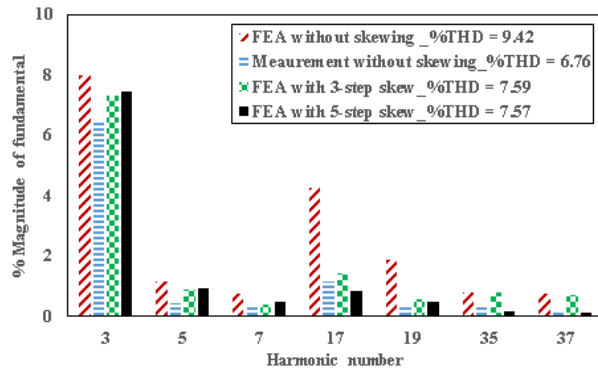


Fig. 2.15. Harmonic order of back EMF at 50% magnetization level.

The slot harmonics from equation (2) are 17th, 19th, 35th and 37th harmonics. The FEA results show that they are notably reduced by the 5-step skewed PM-pole. The FEA results show that the 5th and 7th space harmonics are not significantly affected by skewing.

2.5 TORQUE RIPPLE SUPPRESSION

The torque ripple arises in a balanced electrical machine due to these reasons: (a) space harmonics in the air-gap magneto motive force (MMF) and flux density, (b) magnetic interaction between the PM and slotted stator, (c) field distortion in the air gap and (d) mechanical eccentricity. The torque ripple factor (T_{r-r}) in an electrical machine is defined as the ratio of the peak to peak torque (T_{p-p}) to the average torque (T_{avg}) over one period of electromagnetic torque. The torque ripple factor is given by the equation:

$$T_{r-r} = \frac{T_{p-p}}{T_{avg}} \times 100 \quad (2.3)$$

The VF IPMSM is simulated in JMAG for different levels of magnetization such as 100%, 75%, 50% without skewed and with 3-step and 5-step skewed PM-pole at the rated current in the stator winding. The torque ripple factor is calculated and tabulated for each level of magnetization. The hardware setup to measure the electromagnetic torque of the VF IPMSM at different magnetization levels is shown in Fig. 2.16. The VF IPMSM drives a DC

generator. The VF IPMSM is driven using a PWM inverter. A torque transducer is used to measure the electromagnetic torque at different magnetization levels.



Fig. 2.16. Hardware setup to measure the electromagnetic torque of the VF IPMSM at different magnetization levels.

2.5.A. Torque Ripple Factor With 100% Magnetization

The VF IPMSM is simulated at 100% magnetization level and the rated current in the stator winding without skewed and with 3-step, 5-step skewed PM-pole. The simulated torques with different PM schemes are shown in Fig. 2.17. The measured torque with the unskewed PM-pole is compared to the simulated results. The simulated torque is higher by 6.67% than the measured torque with the unskewed PM-pole. This deviation between the FEA and the measurement occurs as the fundamental component of the back EMF obtained from the FEA is higher compared to the measured back EMF at 100% magnetization level. The fundamental component of the phase back EMF obtained from the FEA without the skewed PM-pole is 144.6 V whereas the measured value is 134.4 V. Higher back EMF results in higher torque. The major harmonic components in each waveform of the torque are shown in Fig. 2.18.

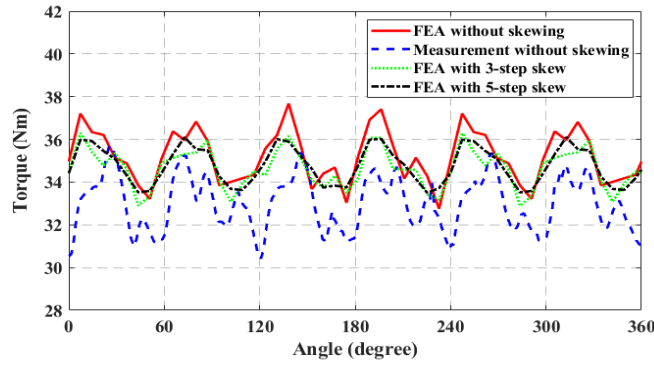


Fig. 2.17. Torque of the VF IPMSM without skewed and with 3-step, 5-step skewed PM-pole for 100% magnetization and skewing angle of $20/3^\circ$.

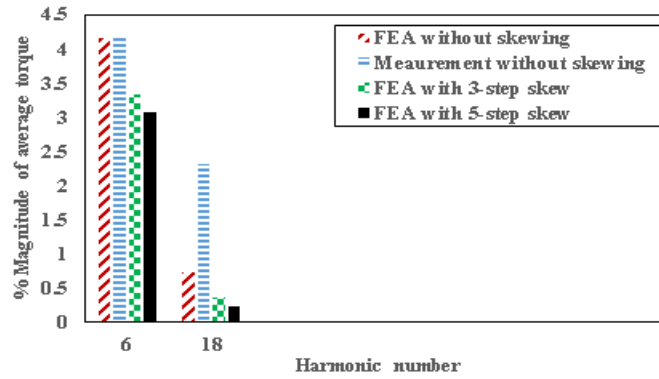


Fig. 2.18. Harmonic order of torque at 100% magnetization level.

The torque ripple factor of the VF IPMSM calculated from Fig. 2.17 using equation (2.3) is mentioned in table 2.2.

Table 2.2: Torque ripple of the VF IPMSM for 100% magnetization

PM scheme	T_{P-P} (Nm)	T_{avg} (Nm)	$T_{r,r}$ (%)
PM without skewing (FEA)	4.9	35.2	13.9
PM without skewing (measurement)	5.3	33.0	16.0
3-step skewed PM with skewing angle $20/3^\circ$ (FEA)	3.4	34.7	9.8
5-step skewed PM with skewing angle $20/3^\circ$ (FEA)	2.6	34.8	7.5

Reduction of torque ripple is more with the 5-step skewed PM-pole than the 3-step skewed PM-pole as observed in table II. Torque ripple is reduced to 9.8% with the 3-step skewed PM-pole and 7.5% with the 5-step skewed PM-pole.

2.5.B Torque Ripple Factor With 75% Magnetization

The simulated electromagnetic torque of the VF IPMSM at rated current and 75% magnetization level is shown in Fig. 2.19 with different PM schemes. The measured torque with the unskewed PM-pole is also shown in the same figure. Fig. 2.19 shows that the simulated torque is higher by 3.8% than the measured torque with the unskewed PM-pole as the fundamental component of the back EMF obtained from the FEA (106.7 V) is higher compared to the measurement (100.9) at 75% magnetization level. The harmonic components of each waveform of torque are shown in Fig. 2.20.

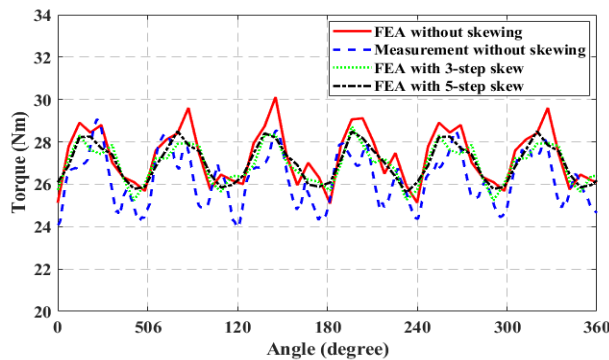


Fig. 2.19. Torque of the VF IPMSM without skewed and with 3-step, 5-step skewed PM-pole for 75% magnetization and skewing angle of $20/3^\circ$.

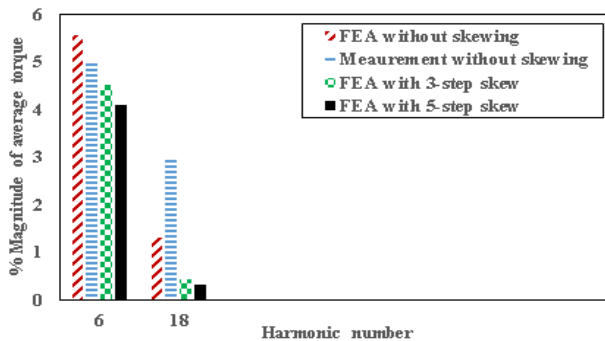


Fig. 2.20. Harmonic order of torque at 75% magnetization level

Table 2.3: Torque ripple of the VF IPMSM for 75% magnetization

PM scheme	T_{avg} (Nm)	T_{rip} (Nm)	$T_{r,r}$ (%)
PM without skewing (FEA)	5.0	27.3	18.3
PM without skewing (measurement)	5.1	26.3	19.4
3-step skewed PM with skewing angle 20/3°(FEA)	3.5	26.9	13.0
5-step skewed PM with skewing angle 20/3°(FEA)	2.9	27.0	10.7

The torque ripple factor of the VF IPMSM at 75% magnetization is mentioned in table 2.3.

The average torque reduces with lower level of magnetization. Therefore, torque ripple is higher for 75% magnetization compared to 100% magnetization. Torque ripple is reduced with both the 3-step and 5-step skewed PM-pole. Torque ripple factor is 13.0% with 3-step skewed PM-pole and 10.7% with 5-step skewed PM-pole.

2.5.C Torque Ripple Factor With 50% Magnetization

The torque of the VF IPMSM is obtained in FEA with 50% magnetized PM at rated current in the stator winding with different PM schemes in Fig. 2.21. The measured torque without skewed PM-pole is also shown in the same figure. The simulated torque follows the measured torque with the unskewed PM-pole as the difference between the fundamental component of the phase back EMF obtained from the FEA (67.6 V) and the measurement (66.2 V) is negligible. The major harmonic components of each waveform are shown in Fig. 2.22. Torque ripple factor of the VF IPMSM at 50% magnetization is given in table 2.4.

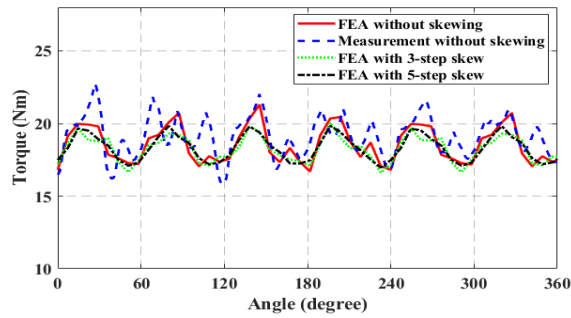


Fig. 2.21. Torque of the VF IPMSM without skewed and with 3-step, 5-step skewed PM for 50% magnetization and skewing angle of $20/3^\circ$.

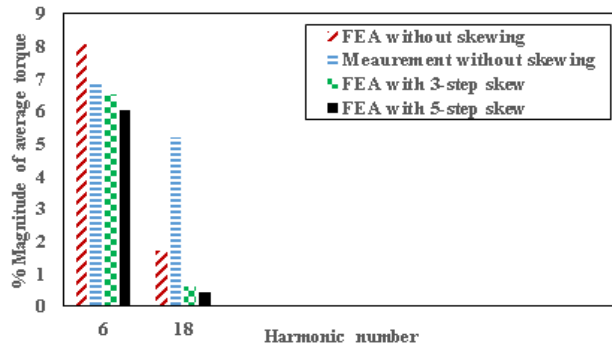


Fig. 2.22. Harmonic order of torque at 50% magnetization level.

Table 2.4: Torque ripple of the VF IPMSM for 50% magnetization

PM scheme	T_{p-p} (Nm)	T_{avg} (Nm)	$T_{r,r}$ (%)
PM without skewing (FEA)	4.6	18.6	24.7
PM without skewing (measurement)	6.9	19.2	36.0
3-step skewed PM with skewing angle $20/3^\circ$ (FEA)	3.5	18.3	19.1
5-step skewed PM with skewing angle $20/3^\circ$ (FEA)	2.9	18.3	15.8

The average torque reduces with the lower levels of magnetization. Therefore, the torque ripple is higher with 50% magnetization compared to 100% or 75% magnetization. The reduction of the torque ripple is higher with the 5-step skewed PM-pole compared to the 3-step skewed PM-pole at 50% magnetization. The torque ripple factor is 19.1% with the 5-step skewed PM-pole and 15.8% with the 3-step skewed PM-pole.

The major harmonic components in the torque are 6th and 18th harmonics. The 6th harmonic is generated due to 5th or 7th harmonics in the back EMF [28]. The 18th harmonic is

generated due to the 17th and 19th harmonics which are the slot harmonics in the back EMF. The FEA results show that the harmonics are minimized with the 3-step and the 5-step skewed PM-pole.

2.6 DEMAGNETIZATION OF PMS

A negative d-axis current pulse is applied to demagnetize the PM-pole permanently in the field weakening region above the base speed. Thus, the efficiency of a VFM can be enhanced when operating above the base speed compared to a PMSM. Six probes are placed along the length of each PM-pole to investigate the demagnetization as shown in Fig. 2.23. Demagnetization of each step of the skewed PM-pole has to be investigated because there is a difference in the angular position between the steps of a skewed PM-pole. A high value of angular deviation between each step causes non-uniform demagnetization of the step skewed PM-pole. So, the minimum optimum skewing angle, $20/3^0$ is chosen to minimize the cogging torque and the torque ripple.

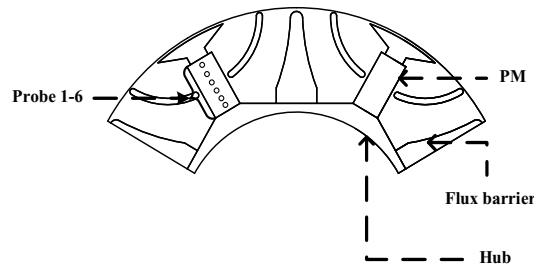


Fig.2. 23. The VF IPMSM with six probes along the length of PM

2.6.A Demagnetization of the unskewed PM-pole

Demagnetization of the unskewed PM-pole is easier compared to the skewed PM-pole. The applied demagnetizing current pulse is shown in Fig. 2.24.

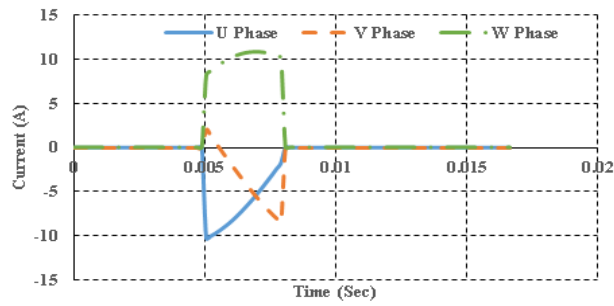


Fig. 2.24. Demagnetizing d-axis current pulse to demagnetize the PMs of the VF IPMSM.

The flux density of the unskewed PM-pole before and after applying the demagnetizing current pulse is shown in Fig. 2.25. The demagnetizing current pulse brings the magnetic flux density close to zero which ensures complete demagnetization of the unskewed PM-pole of the VF IPMSM. The FEA results in Fig. 2.26 show that both the PMs are uniformly demagnetized.

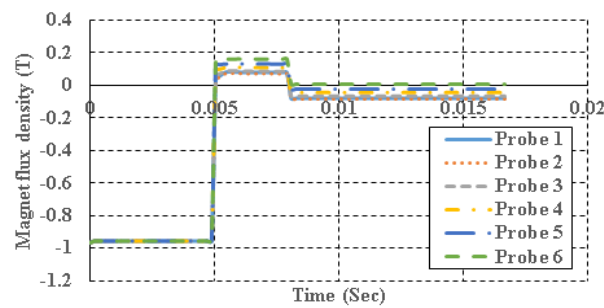


Fig. 2.25. Magnet flux density of the VF IPMSM before and after applying the demagnetizing current pulse.

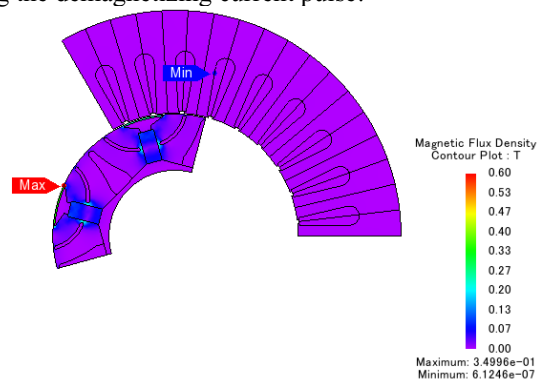


Fig. 2.26. Magnet flux distribution of the unskewed PM-pole after removing the applied demagnetizing d-axis current.

2.6.B Demagnetization of the 3-step skewed PM-pole

Each step of the 3-step skewed PM-pole in the VF IPMSM has to be demagnetized uniformly. Analytical model of the local demagnetization in VFM due to armature winding MMF was analyzed in [27]. The demagnetizing current pulse shown in Fig. 2.24 is also applied to the 3-step skewed PM-pole with respect to the 2nd step of the skewed PM-pole. The 2nd step is aligned with the d-axis. The angular difference between the 1st and 3rd step and the d-axis armature field is equal. Therefore, applying the demagnetization current pulse will result in a uniform demagnetization in the 1st and 3rd steps. The magnetic flux density of the 1st, 2nd and 3rd step of the skewed PM-pole before and after applying the demagnetizing current pulse are shown for skewing angles of $20/3^0$, $40/3^0$ in Fig. 2.27, 2.28 and 2.29 respectively.

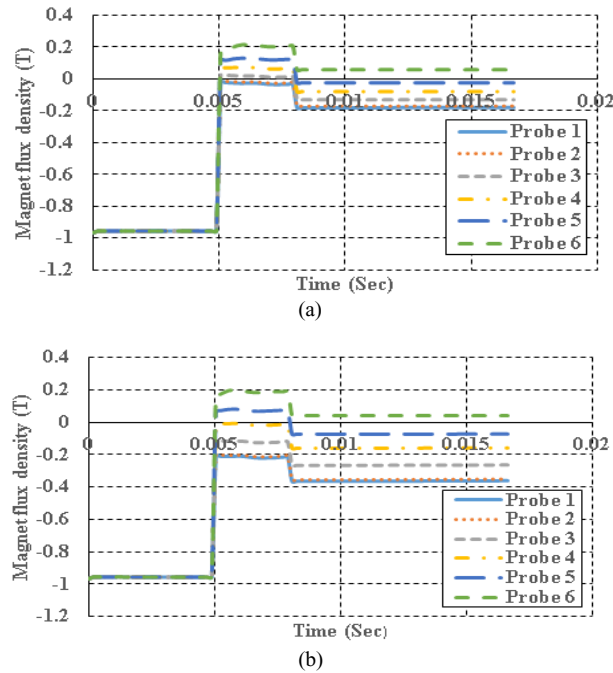


Fig. 2.27. Magnet flux density of 1st step of 3-step skewed PM-pole before and after applying demagnetizing current pulse for skewing angle (a) $20/3^0$ (b) $40/3^0$.

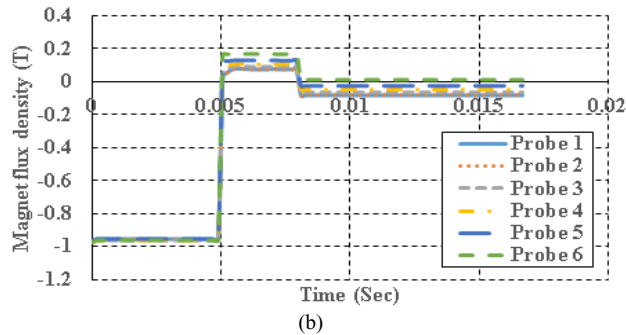
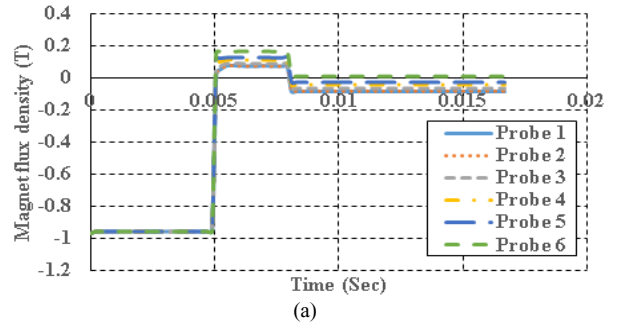


Fig. 2.28. Magnet flux density of 2nd step of 3-step skewed PM-pole before and after applying demagnetizing current pulse for skewing angle (a) $20/3^0$

The results show that the magnetic flux density of each step of the 3-step skewed PMs is close to zero for a skewing angle of $20/3^0$ after the demagnetization. So, each step of the 3-step skewed PM-pole is demagnetized with less non-uniformity for a skewing angle of $20/3^0$. The 2nd step of the 3-step skewed PM-pole in Fig. 2.28(b) is demagnetized completely for a skewing angle of $40/3^0$. But the magnetic flux density of the 1st and 3rd steps in Fig. 2.27(b) and 2.29(b) respectively are not close to zero for a skewing angle of $40/3^0$ and they are demagnetized with more non-uniformity. Therefore, the skewing angle of $20/3^0$ is preferable compared to $40/3^0$.

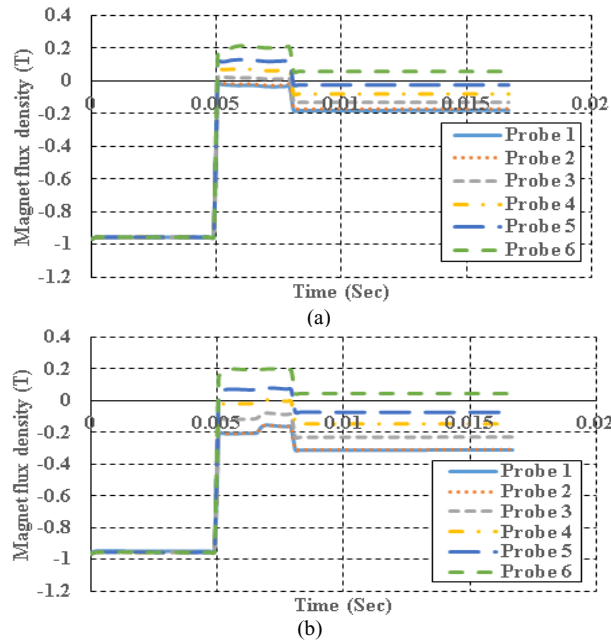


Fig. 2.29. Magnet flux density of 3rd step of 3-step skewed PM-pole before and after applying demagnetizing current pulse for skewing angle (a) 20/3° (b) 40/3°.

2.7 MAGNETIZATION OF PMS

The magnetization of the unskewed and 3-step skewed PM-pole is explained in this section. The magnetization of the 3-step skewed PM-pole is performed with the minimum optimum skewing angle, 20/3°. Similar to the FEA simulation of demagnetization, six probes are placed along the length of each PM-pole to measure the magnet flux density.

2.7.A Magnetization of the unskewed PM-pole

A d-axis current pulse (pulse 1) is applied to demagnetize the PM-pole and another current pulse (pulse 2) is applied to magnetize the PM as shown in Fig. 2.30. Magnetization current is higher compared to the demagnetizing current. The flux density of the PM-pole after magnetization is shown in Fig. 2.31. The FEA results show that the unskewed PM-pole is magnetized to 100% magnetization level.

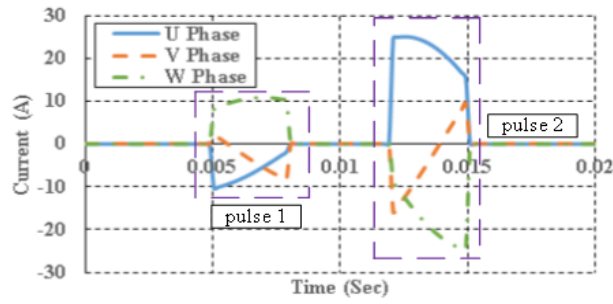


Fig. 2.30. Pulse 1 represents demagnetizing d-axis current, and pulse 2 represents magnetizing d-axis current.

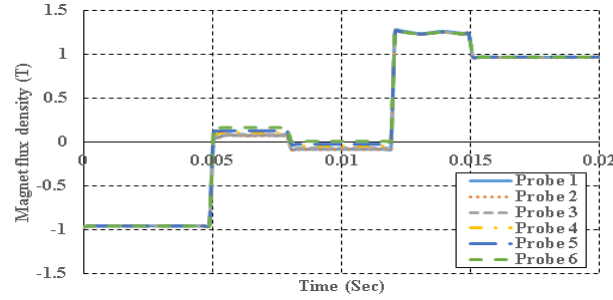


Fig. 2.31. Magnet flux density of the VF IPMSM after applying the magnetizing current pulse.

2.7.B Magnetization of the 3-step skewed PM-pole

The magnetizing current pulse shown in Fig. 2.30 is applied to the 3-step skewed PM-pole with respect to the 2nd step of the skewed PM-pole. The magnetic flux density of the 1st, 2nd and 3rd step of the skewed PM-pole after magnetization are shown in Fig. 2.32, 2.33 and 2.34 respectively for the skewing angle of $20/3^{\circ}$. The FEA results show that each step of the 3-step skewed PM-pole can be magnetized to 100% magnetization with proper magnitude of the d-axis current.

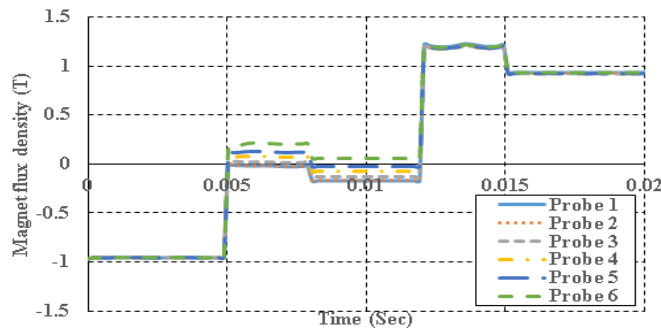


Fig. 2.32. Magnet flux density of 1st step of 3-step skewed PM-pole before and after applying magnetizing current pulse for skewing angle $20/3^{\circ}$.

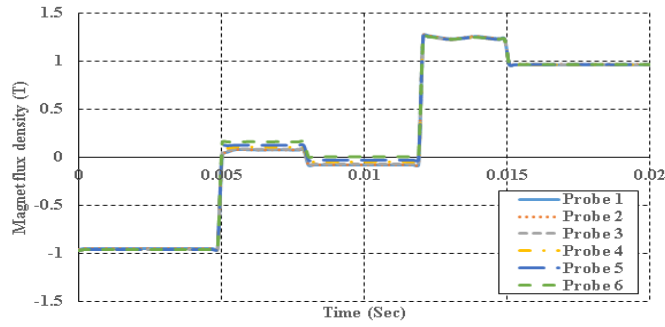


Fig. 2.33. Magnet flux density of 2nd step of 3-step skewed PM-pole before and after applying magnetizing current pulse for skewing angle 20/3°.

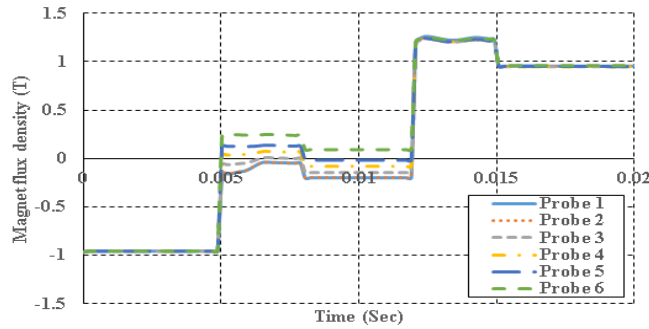


Fig. 2.34. Magnet flux density of 3rd step of 3-step skewed PM-pole before and after applying magnetizing current pulse for skewing angle 20/3°.

2.8 CONCLUSIONS

This work reduces the cogging torque and hence the torque ripple in a 27 slot 6 pole VF IPMSM by step skewing the PMs. The cogging torque of the VF IPMSM is shown with different magnetization levels. The magnitude of the cogging torque increases with higher magnetization level. The cogging torque reduction is higher for optimum skewing angle with a 5-step skewed PM-pole than a 3-step skewed PM-pole at 100% magnetization. The FEA results show that skewing effect notably minimizes the slot harmonics in the back EMF.

Torque ripple reduction is higher with a 5-step skewed PM-pole compared to a 3-step skewed PM-pole at each level of magnetization. The torque ripple is reduced by 6.4% at 100% magnetization, 7.6% at 75% magnetization and 8.9% at 50% magnetization with a 5-step skewed PM-pole. Therefore, the torque ripple reduction is higher at lower levels of magnetization. The average torque reduces with lower magnetization levels. Therefore,

torque ripple increases with lower magnetization levels. The FEA and hardware results of the cogging torque for the unskewed rotor VF IPMSM are compared at 100% magnetization level. There is a rotor eccentricity in the VF IPMSM at 100% magnetization level and this can be the cause of the difference between measured and FEA results.

The unskewed PM-pole is demagnetized by applying a current pulse. The magnetic flux density of each step of the 3-step PM-pole can be brought close to zero with a current pulse for a skewing angle of $20/3^{\circ}$ compared to a skewing angle of $40/3^{\circ}$. Therefore, a skewing angle of $20/3^{\circ}$ is preferable. There is no requirement of additional demagnetizing current for the step skewed PM-pole. The FEA results show that the unskewed as well as the 3-step skewed PM-pole is magnetized with a current pulse.

This chapter focused on a variable flux machine with Alnico magnet, the next chapter considers a more complex variable flux machine with an Alnico magnet and a rare earth magnet in series.

Chapter 3

Cogging Torque Analysis in a Series Hybrid Variable Flux Machine using Lumped Magnetic Circuits

3.1 INTRODUCTION

The conventional permanent magnet synchronous machines (PMSMs) with rare earth magnets have challenges in wide speed region due to requirement of a continuous d-axis demagnetizing current in the field weakening operation [29]. The demagnetizing d-axis current causes additional copper loss of the rare earth PMSMs. In order to enhance the wide speed region, a variable flux machine (VFM) using lower coercive force magnet AlNiCo9 was proposed [4], [6], [30]-[32] where the d-axis demagnetizing current was reduced significantly. However, the lower coercive force AlNiCo9 magnet is prone to armature demagnetization field. On the other hand, in a 36-slot 6-pole SVFM in [33], the higher coercive force N48SH magnet raised the operating point of the lower coercive force AlNiCo9 magnet, thus improving the machine performance with a stable field weakening operation.

One of the major problem of the 36-slot 6-pole SVFM is cogging torque. Cogging torque is the no load reluctance torque due to the magnetic attraction between the permanent magnets (PMs) and slotted stator at no load. The cogging torque causes torque ripple and does not contribute to the net effective torque [15]. Therefore, it is very essential to calculate the value of the cogging torque in the 36-slot 6 pole SVFM. The analytical models for predicting the cogging torque in surface-mounted permanent-magnet machines (SPMSMs), viz., lateral force, complex permeance, and exact subdomain models, together with a subdomain model based on a single slot/pole were analyzed in [34]. A simple analytical technique was proposed to synthesize the cogging-torque waveform of a permanent magnet brushless machine from the cogging torque, which is associated with a single stator slot [35]. A method for predicting the cogging torque in radial field permanent magnet brushless

motors, based on the analytical calculation of the air gap field distribution and the net lateral force acting on the stator teeth, was developed and validated [36].

The cogging torque of the 36-slot, 6-pole SVFM is computed using a Fourier series expansion of the air gap flux density in an equivalent slot-less machine and the relative air gap permeance function [11], [18]. The air gap flux density is calculated using a lumped magnetic circuit model in this article. Although the FEA can accurately calculate the flux density distribution in the air gap, it often requires a higher computation time to verify a design. Therefore, a lumped magnetic circuit model [37]-[40] can be a trade between computation time and accuracy to calculate the air gap flux density. A simple lumped magnetic circuit model for interior permanent-magnet (IPM) machines with multi-segment and multilayer permanent magnets was presented in [41]. The open-circuit air-gap field distribution, average air gap flux density, and leakage fluxes were derived analytically. The cogging torque waveform of the interior permanent magnet (IPM) machine was predicted using only an analytical model based on the proposed virtual permanent magnet (PM) concept, IPM was considered as surface PM having zero height and unit relative permeability [42]. A new analytical model for estimating the cogging torque in a multi flux-barrier interior permanent magnet machine (IPM) based on a lumped magnetic circuit considered the saturated bridge in the rotor's iron core [43].

This work calculates the open circuit air gap flux density using a lumped magnetic circuit in the slot-less 6-pole SVFM at different magnetization levels of the AlNiCo9 magnet. The higher coercive force N48SH magnet is in series with the lower coercive force AlNiCo9 magnet to improve the machine performance with a stable field weakening operation. The lumped magnetic circuit is developed based on the magnetic flux lines obtained in the FEA.

The developed lumped magnetic circuit considered the saturated bridge in the rotor's iron core. The computed air gap flux density in the slot-less SVFM is compared to the FEA results at 100%, 75%, and 50% magnetization levels of the AlNiCo9 magnet. Thus, the magnetic circuit model is validated. The cogging torque is computed based on the Fourier series of the air gap flux density in an equivalent slot-less machine and the relative air gap permeance function and compared to the FEA results at different magnetization levels of the AlNiCo9 magnet.

3.2 LUMPED MAGNETIC CIRCUIT OF THE SVFM

The greatest common divisor of the number of slot (36) and pole (6) is 6. Therefore, the 36-slot 6-pole SVFM has a magnetic symmetry of mechanical 60 degree. A two-dimension (2-D) section of mechanical 60 degree of the slot-less SVFM is shown in Fig. 3.1. Each section consists of 6 slot and one pole. Each pole consists of two segments of magnet, PM1 and PM2. In each segment, the higher coercive force N48SH magnet is in series with the lower coercive force AlNiCo9 magnet to improve the machine performance with a stable field weakening operation. The lumped magnetic circuit of the 36-slot 6-pole SVFM is developed based on the analysis of flux lines obtained in FEA in a slot-less machine and Kirchhoff's law is applied for deriving the analytical expressions of the fluxes. The slot-less stator core, rotor core including iron bridge, PM1 and PM2 are also shown in Fig. 3.1. The leakage fluxes of the PM1 and PM2 through the iron bridges of the rotor core are shown in the same figure. The required dimensions to compute the magnetic parameters of the lumped magnetic circuit of the SVFM are provided in Fig. 3.2. The major dimensions which can affect the fluxes are chosen based on analysis of the flux lines in the SVFM obtained in FEA in Fig. 3.1. Thus, the open circuit air gap flux density, leakage fluxes of magnet over one

pole, magnet end leakage fluxes in the 36-slot 6-pole SVFM can be computed by using the lumped magnetic circuit model.

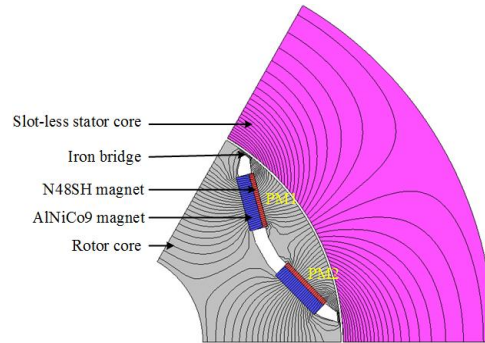


Fig. 3.1. Flux lines in the SVFM.

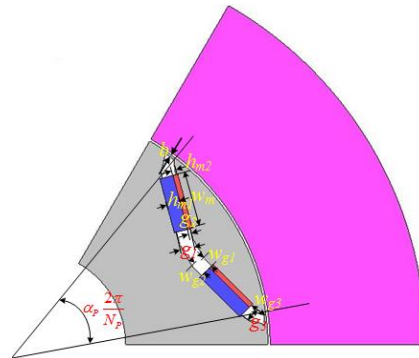


Fig. 3.2. Dimensions of the slot-less 6-pole SVFM.

The open circuit air gap flux density in the SVFM is computed using the developed lumped magnetic circuit as shown in Fig. 3.3. The detail of the lumped magnetic circuit is discussed here. ϕ_{r1} and ϕ_{r2} , and ϕ_{mo1} and ϕ_{mo2} are the sources of flux and the leakage fluxes of the AlNiCo9 and the N48SH magnet over one pole, the corresponding leakage flux reluctances being R_{mo1} and R_{mo2} . ϕ_{mb} is the leakage flux through the iron bridge of the rotor core and R_{bm} is the bridge reluctance. ϕ_{1ml1} , ϕ_{2ml1} and ϕ_{1ml2} , ϕ_{2ml2} are the magnet end leakage fluxes of the AlNiCo9 and the N48SH magnet where R_{1ml1} , R_{2ml1} and R_{1ml2} , R_{2ml2} are the corresponding leakage reluctances through air. The stator and rotor yoke are made of

M3629G laminated steel. In general, there is negligible saturation in the stator and rotor yoke due to the high permeability of the steel material, stator and rotor reluctances are neglected to compute the open circuit air gap flux density.

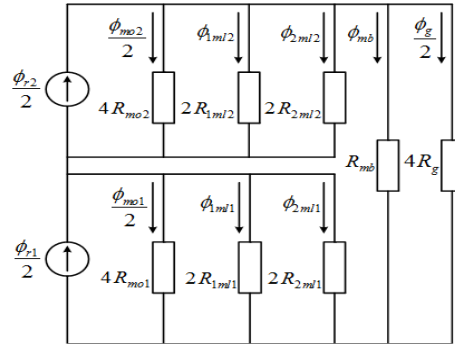


Fig. 3.3. Lumped magnetic circuit of the SVFM.

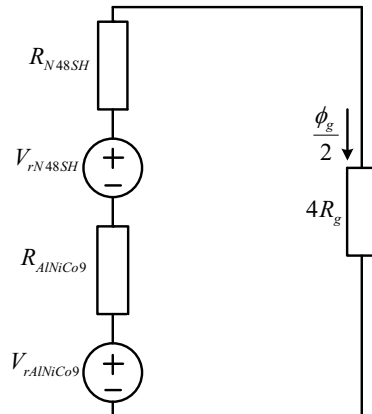


Fig. 3.4. Simplified lumped magnetic circuit of the SVFM.

In reference to the Fig. 3.1, the following equations can be easily obtained:

$$\phi_{r1} = 2 B_{rAlNiCo9} A_m = 2 B_{rAlNiCo9} w_m L \quad (3.1)$$

$$\phi_{r2} = 2 B_{rN48SH} A_m = 2 B_{rN48SH} w_m L \quad (3.2)$$

$$R_g = \frac{g}{\mu_o A_g} \quad (3.3)$$

$$R_{m o 1} = \frac{h_{m 1}}{\mu_o \mu_{r A l N i C o 9} A_m} = \frac{h_{m 1}}{\mu_o \mu_{r A l N i C o 9} w_m L} \quad (3.4)$$

$$R_{m o 2} = \frac{h_{m 2}}{\mu_o \mu_{r N 48 S H} A_m} = \frac{h_{m 2}}{\mu_o \mu_{r N 48 S H} w_m L} \quad (3.5)$$

$$A_g = \alpha_p \frac{2\pi \left(R_i - \frac{g}{2} \right)}{N_p} L \quad (3.6)$$

$$R_{1 m 1 1} = \frac{g_3}{\mu_o L w_{g 3}} \quad (3.7)$$

$$R_{2 m 1 1} = \frac{g_3}{\mu_o L \left(\frac{w_{g 1} + w_{g 2}}{2} \right)} \quad (3.8)$$

$$R_{1 m 1 2} = \frac{g_2}{\mu_o L w_{g 3}} \quad (3.9)$$

$$R_{2 m 1 2} = \frac{g_2}{\mu_o L \left(\frac{w_{g 1} + w_{g 2}}{2} \right)} \quad (3.10)$$

Where μ_o is the permeability of air, $\mu_{r A l N i C o 9}$ is the relative recoil permeability of the AlNiCo9 magnet, $\mu_{r N 48 S H}$ is the relative recoil permeability of the N48SH magnet; $B_{r A l N i C o 9}$ is the remanence of AlNiCo9 magnet, $B_{r N 48 S H}$ is the remanence of the N48SH magnet, g is the air gap length, A_g is the air gap area, L is the length of the machine in the z direction, R_i is the stator bore radius. In each segment, $h_{m 1}$ and $h_{m 2}$ are the length of the AlNiCo9 magnet and the N48SH magnet respectively, whereas the width of each magnet is w_m . The bridge reluctance (R_{bm}) is nonlinear due to saturation in the bridge and taken into account to compute the open

circuit air gap flux density in a slot-less machine. Leakage flux through the bridge can be approximately computed as follows:

$$\phi_{mb} = B_{sat} A_b$$

Where $A_b = bL$ provides the cross-section area of the bridge, b is the bridge width and B_{sat} is the saturated magnetic flux density of the laminated core material in the bridge, where $B_{sat} = 2.2$ T.

The bridge flux is modeled parallel with the N48SH and AlNiCo9 magnet fluxes to make the calculation of the air-gap flux density easier using the lumped magnetic circuit model. The lumped magnetic circuit model of the 36-slot 6-pole SVFM is derived based on flux lines shown in Fig. 3.1. The N48SH magnet material is in series with the AlNiCo9 magnet to reduce the effect of armature demagnetizing field. The open circuit air-gap magnetic flux density of the SVFM is computed at different magnetization levels of AlNiCo9 magnet. The open circuit air-gap flux density of the SVFM at different magnetization levels of the AlNiCo9 magnet is calculated using the lumped magnetic circuit model in Fig. 3.3. The flux sources are converted into MMF sources for each magnet in a segment. Thus, the lumped magnetic circuit model can be further simplified to compute the air gap flux density in Fig. 3.4.

The AlNiCo9 and N48SH magnet are represented by flux sources ϕ_{r1} and ϕ_{r2} respectively. Both magnets are converted to equivalent MMF (magneto motive force) sources $V_{rAlNiCo9}$ and V_{rN48SH} respectively to make the computation of the air-gap flux density easier. $R_{AlNiCo9}$ and R_{N48SH} in Fig. 3.4 are the equivalent leakage reluctances of the AlNiCo9 and the N48SH magnet respectively. The air gap flux density is computed utilizing the simplified lumped magnetic circuit model in Fig. 3.4 and the following equations.

$$\frac{1}{R_{AlNiCo9}} = \frac{1}{4R_{m01}} + \frac{1}{2R_{1m11}} + \frac{1}{2R_{2m11}} \quad (3.11)$$

$$\frac{1}{R_{N48SH}} = \frac{1}{4R_{m02}} + \frac{1}{2R_{1m12}} + \frac{1}{2R_{2m12}} \quad (3.12)$$

$$V_{rAlNiCo9} = \frac{\phi_{r1}}{2} R_{AlNiCo9} \quad (3.13)$$

$$V_{rAlNiCo9} = \left(\frac{\phi_{r2}}{2} - \phi_{mb} \right) R_{N48SH} \quad (3.14)$$

$$\frac{\phi_g}{2} = \frac{kV_{rAlNiCo9} + V_{rN48SH}}{R_{AlNiCo9} + R_{N48SH} + 4R_g} \quad (3.15)$$

$$B_g = \frac{\phi_g}{A_g} \quad (3.16)$$

Where k indicates the magnetization level of the AlNiCo9 magnet. The design parameters of the 6-pole SVFM are provided in Table 3.1. The open circuit air-gap flux density of the SVFM with 100%, 75% and 50% magnetization levels of AlNiCo9 magnet are provided in Fig. 3.5, 3.6 and 3.7 respectively and compared to the FEA results. The comparison between FEA and analytical result is shown in Table 3.2.

TABLE 3.1: MACHINE DESIGN PARAMETERS

$B_{rAlNiCo9} (T)$	1.09	$h_{m1} (mm)$	3.12089	$g_2 (mm)$	3.22994
$\mu_{rAlNiCo9}$	1.1567	$h_{m2} (mm)$	1.10906	$W_{g1} (mm)$	2.48958
$B_{rN48SH} (T)$	1.39	$w_m (mm)$	12.83085	$W_{g2} (mm)$	2.96305
μ_{rN48SH}	1.00	$L (mm)$	125	$W_{g3} (mm)$	3.47778
$B_{sat} (T)$	2.3	$g (mm)$	0.5	$b (mm)$	0.5
$R_1 (mm)$	54.25	$g_1 (mm)$	3.23003	N_p	6
α_p	0.75	$g_2 (mm)$	0.60906	N_s	36

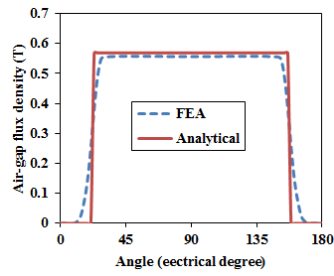


Fig. 3.5. Flux density comparison at 100% magnetization level

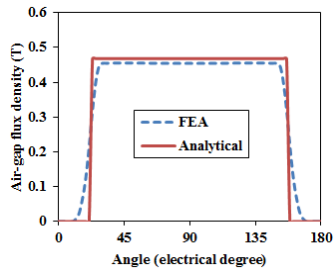


Fig.3.6. Flux density comparison at 75% magnetization level.

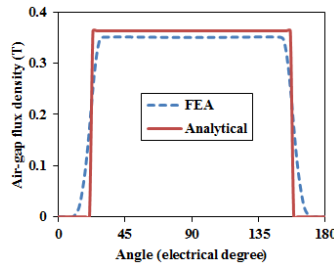


Fig. 3.7. Flux density comparison at 50% magnetization level

Table 3.2: AIR GAP FLUX DENSITY

Magnetization level of AlNiCo9 magnet (%)	B_z (T) (FEA)	B_z (T) (Analytical)	Error (%)
100	0.5589	0.5703	2.04
75	0.4559	0.4681	2.61
50	0.3515	0.3629	3.25

It is observed in Table 3.2 that there is an insignificant difference between FEA, and analytical results and the error is within 4% at different magnetization levels. The percentage error increases at lower level of magnetization of the AlNiCo9 magnet.

3.3 COGGING TORQUE ANALYSIS

Cogging torque of the 36-slot 6-pole SVFM is analyzed at different magnetization levels of the AlNiCo9 magnet in the next section. The flux density at different magnetization levels computed in the above section are used to calculate the cogging torque of the SVFM. This research work computes the cogging torque at different magnetization levels of the AlNiCo9 magnet for example at 100%, 75% and 50% in the 36-slot, 6-pole SVFM where the higher coercive force N48SH magnet material is in series with the lower coercive force AlNiCo9 magnet to reduce the effect of armature demagnetizing field. The general expression of cogging torque is given in [11], [13], [44] – [47] as

$$T_{cog}(\alpha) = \frac{\pi L N_L (R_2^2 - R_1^2)}{4 \mu_o} \sum_{n=1}^{\infty} n G_{anN_L} B_{anN_L} \sin(n N_L \alpha) \quad (3.17)$$

Where R_2 and R_1 are the outer and inner radius of air gap respectively; N_L is the least common multiple of number of slot and pole and the period of cogging torque. L is the stack length of the SVFM, G_{anN_L} and B_{anN_L} are the Fourier coefficients of the air gap permeance function and the air gap flux density function in an equivalent slot-less machine respectively. The cogging torque in (3.17) is derived using the energy method based on the Fourier transform of the air gap flux density in an equivalent slot-less machine and the relative air gap permeance function. However, the air gap flux density at each magnetization level of the AlNiCo9 magnet is required to compute the cogging torque. The air gap flux density at different magnetization levels is computed using the lumped magnetic circuit developed in this research work. The relative air gap permeance function is discussed in detail in the next section.

The greatest common divisor of the number of slot and pole in the 36-slot 6-pole SVFM is 6. Therefore, the SVFM has a magnetic symmetry of mechanical 60° . However, $1/6^{\text{th}}$ of the 36-slot, 6-pole SVFM is shown in Fig. 3.8. The distribution of the magnetic flux density vector in different parts of the SVFM obtained using JMAG at 100% magnetization of the AlNiCo9 magnet and no load is provided in Fig. 3.9. Similarly, the FEA analysis of the SVFM at 50% magnetization level can be simulated. The specification of the SVFM is provided in detail in Table 3.3.

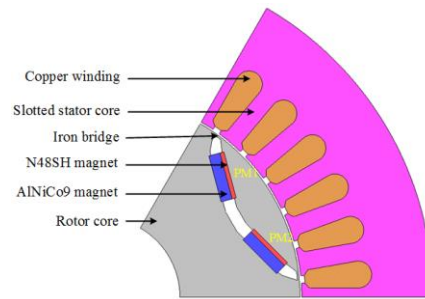


Fig. 3.8. $1/6^{\text{th}}$ of the 36-slot 6-pole SVFM.

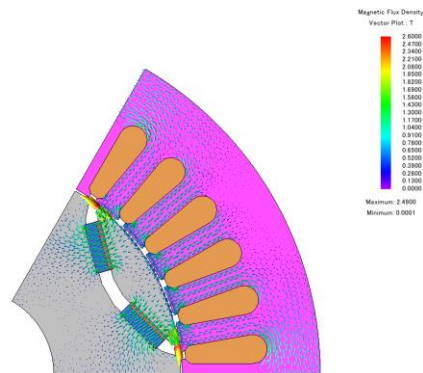


Fig. 3.9. Magnetic flux density vector plot of the 36-slot 6-pole SVFM at 100% magnetization and no load.

Table 3.3: SPECIFICATIONS OF THE 36-SLOT 6-POLE SVFM

Machine parameters	Machine specification
Rated power (kW)	8.5
DC bus voltage (V)	600
Rated speed (rpm)	1800
Rated current (A)	17
Magnetizing current (A)	31.5
Outer diameter (mm)	180
Inner diameter (mm)	108

3.4 FOURIER COEFFICIENTS

In this section, the Fourier coefficients in (3.17) are derived based on air gap flux density in an equivalent slot-less machine and relative air gap permeance. The leakage flux of the PM-pole is neglected and ideal air gap flux density at 100%, 75%, 50% magnetization levels of AlNiCo9 magnet are considered to find the Fourier coefficients. The air gap permeance function is required to define correctly to compute the cogging torque at the different magnetization levels. The relative air gap permeance function is defined in (3.18) as a function of magnet height (h_m), air gap (g), and magnet recoil permeability (μ_r), the circumferential length of PM field along the sides of a slot (r_s).

$$G(\theta) = \frac{g + \frac{h_{m1}}{\mu_{rAlNiCo9}} + \frac{h_{m2}}{\mu_{rN48SH}}}{g + \frac{h_{m1}}{\mu_{rAlNiCo9}} + \frac{h_{m2}}{\mu_{rN48SH}} + \frac{2\pi r_s}{4}} \quad (3.18)$$

Where $G(\theta)$ is the relative air gap permeance function.

3.4.A Determination of G_{anNL}

A slot is shown in Fig. 3.10(a) and the corresponding simplest relative air gap permeance function is shown in Fig. 3.10(b). The relative air gap permeance function is utilized to compute the cogging torque of the 36-slot 6-pole SVFM at different magnetization levels of the AlNiCo9 magnet.

Fourier coefficient of the relative air gap permeance function in (3.17) for the symmetrically distributed PM machine with PM-pole on a rotor is obtained as follows.

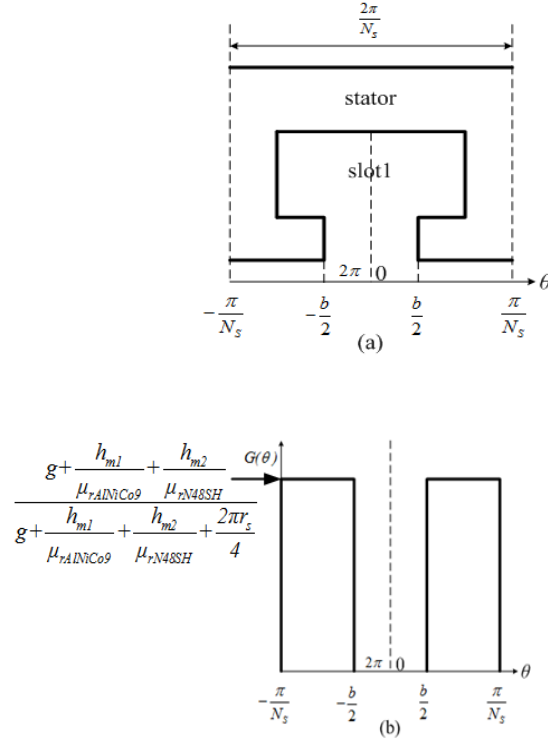


Fig. 3.10. Simplified model: (a) a slot and (b) corresponding relative air gap permeance.

$$\begin{aligned}
 G(\theta) &= \frac{N_s}{\pi} \left[\frac{g + \frac{h_{m1}}{\mu_{rAlNiCo9}} + \frac{h_{m2}}{\mu_{rN48SH}}}{g + \frac{h_{m1}}{\mu_{rAlNiCo9}} + \frac{h_{m2}}{\mu_{rN48SH}} + \frac{2\pi r_s}{4}} \right]^2 \\
 &\times \left[\int_{-\frac{\pi}{N_s}}^{-\frac{b}{2}} \cos(nN_L\theta) + \int_{\frac{b}{2}}^{\frac{\pi}{N_s}} \cos(nN_L\theta) \right] \\
 &= -\frac{2N_s}{\pi nN_L} \left[\frac{g + \frac{h_{m1}}{\mu_{rAlNiCo9}} + \frac{h_{m2}}{\mu_{rN48SH}}}{g + \frac{h_{m1}}{\mu_{rAlNiCo9}} + \frac{h_{m2}}{\mu_{rN48SH}} + \frac{2\pi r_s}{4}} \right]^2 \sin\left(\frac{nN_L b}{2}\right)
 \end{aligned} \tag{19}$$

Where b is the slot opening and N_s is the number of slots.

3.4.B Determination of B_{anNL}

The ideal distribution of the flux density in the air gap due to one PM-pole in a slot-less PM machine is shown in Fig. 3.11. The fringing effect for the inter-pole magnet is neglected and leakage flux is considered zero during the derivations. Therefore, the air-gap flux density is constant over the pole arc, and it is given by B_0 .

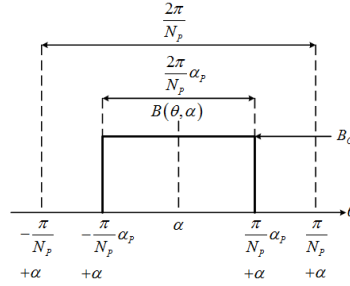


Fig. 3.11. Ideal distribution of air-gap flux density for one PM-pole.

where N_p is the number of poles and α is the rotational angle of the rotor. Fourier coefficient of the ideal air gap flux density in (17) for the symmetrically distributed PM machine with PM-pole on the rotor is derived in this section. It is observed that B_{anNL} can be calculated as follows (20).

$$B_{anN_L} = \frac{N_p}{\pi} \left[\int_{-\frac{\pi}{N_p} + \alpha}^{\frac{\pi}{N_p} - \alpha} B_0 \cos(nN_L(\theta)) d\theta \right]$$

$$= \frac{2N_p B_0^2}{\pi nN_L} \sin \left(nN_L \left(\frac{\pi}{N_p} \alpha_p \right) \right) \quad (20)$$

3.5 EXPERIMENTAL SETUP

This section describes the hardware setup for the cogging torque measurement. The hardware setup consists of a torque arm, torque transducer and the test SVFM and dynamometer. The model number of the torque transducer is T8-5-1A1. The interface torque transducer has a torque capability of 5 Nm with 5 V DC output voltages. The accuracy of the torque transducer is 0.25%. The torque transducer is connected to a personal computer to collect the measured torque values. Cogging torque of the SVFM is measured at 50% and 100% magnetization levels of the AlNiCo 9 magnet and compared to the FEA and analytical results. Cogging torque at 50% and 100% magnetization levels are measured by rotating the shaft by the torque arm shown in Fig. 3.12

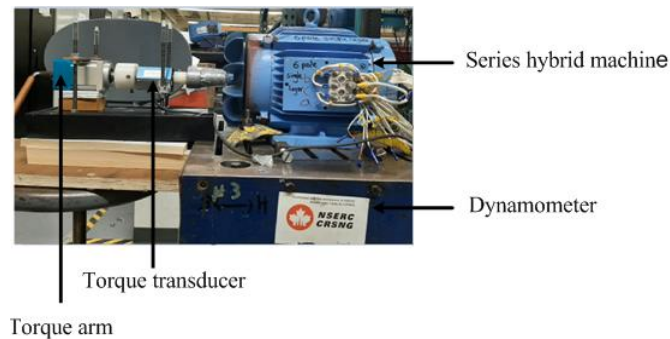


Fig. 3.12. Hardware setup to measure cogging torque.

3.6 COMPUTATION OF COGGING TORQUE

The Fourier coefficients of air gap flux density and air gap permeance function derived in (3.19) and (3.20) respectively are utilized in (3.17) to find the cogging torque at each magnetization level of the AlNiCo9 magnet in the 36-slot 6-pole SVFM. The cogging torque of the SVFM is computed and compared to the FEA results at 100% and 50% magnetization levels of the AlNiCo9 magnet in Fig. 3.13 and 3.14. Measurement of cogging torque at 100%

and 50% magnetization levels are also shown in Fig. 3.13 and 3.14. Thus analytically computed and FEA values of cogging torque are validated by measurement.

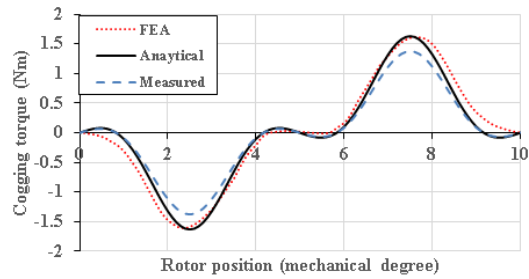


Fig. 3.13. Cogging torque comparison at 100% magnetization of AlNiCo9 magnet.

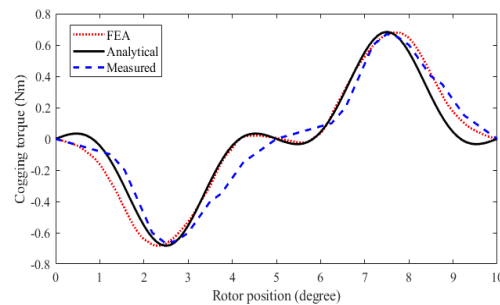


Fig. 3.14. Cogging torque comparison at 50% magnetization of AlNiCo9 magnet.

Therefore, cogging torque comparison of FEA and analytical results at 100% and 50% magnetization levels are validated by measurements.

3.7 EFFECT OF COGGING TORQUE

3.7.A Back EMF

Effect of cogging torque on the back EMF of the 36-slot SVFM at 100%, 75% and 50% magnetization levels are investigated in this work. The cogging torque introduces slot harmonics in the back EMF waveform and enhances the torque ripple. The percentage THD of the back EMF waveform in Fig. 3.15 will be analyzed at 100%, 75% and 50% magnetization levels in detail. The THD of the back EMF is higher at lower level of magnetizations as shown in table 3.4 as the fundamental peak reduces with lower magnetization levels. The peak value of the fundamental at 100% magnetization is 130.3 V

whereas peak value of fundamental at 75 % magnetization is 104.5V and 83.6 at 50% magnetization. The cogging torque causes 11th, 13th, 23rd, 25th, 35th harmonics which enhances the torque ripple of the 36-slot SVFM.

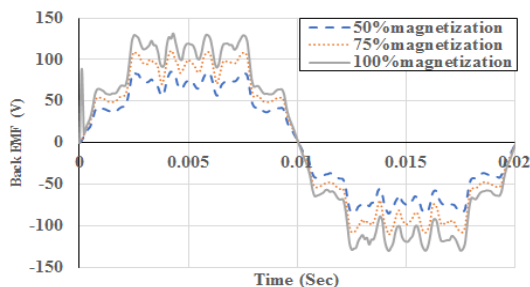


Fig. 3.15. Back EMF at different magnetization levels.

Table 3.4: EFFECT OF COGGING TORQUE ON Back EMF

Harmonic number (%)	50% magnetization	75% magnetization	100% magnetization
3 rd	12.6	12.3	12
7 th	3.4	3.5	3.75
9 th	10.2	10	10
11 th	5	4.25	3.75
13 th	6.8	6.4	5.5
23 rd	6.1	6.4	6.2
25 th	4.2	4.6	4.75
35 th	1.8	1.75	2.2
THD	20.34	19.96	19.94

3.7.B Electromagnetic torque

Effect of cogging torque on the electromagnetic torque of the 36-slot SVFM at 100%, 75% and 50% magnetization levels are investigated in this work. The electromagnetic torque is simulated with rated current in the winding at each magnetization levels. The cogging torque introduces slot harmonics in the back EMF waveform and enhances the torque ripple. The percentage THD of the electromagnetic torque waveform in Fig. 3.16 will be analyzed at 100%, 75% and 50% magnetization levels in detail. The THD of the electromagnetic is higher at lower level of magnetizations as shown in table 3.5 as the average value of the torque reduces with lower magnetization levels. The average value of the fundamental at 100% magnetization is 41.04 V whereas the average value of fundamental at 75% magnetization is 39.2 and 36.65 at 50% magnetization. The cogging torque causes 11th, 13th,

23rd, 25th, 35th harmonics in back EMF which enhances the torque ripple of the 36-slot SVFM. The 6th harmonic in the torque waveform is generated by spatial 5th and 7th harmonics in the back EMF. The cogging torque mainly causes the 12th, 24th and 36th harmonics in the output electromagnetic torque waveform. Thus, it is observed that cogging torque has a major impact on the quality of output torque waveform.

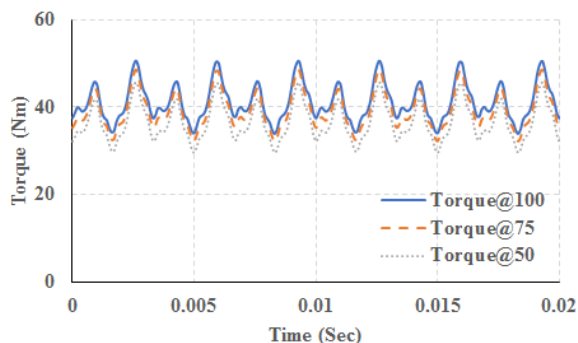


Fig. 3.16. Torque at different magnetization levels.

Table 3.5: EFFECT OF COGGING TORQUE ON TORQUE

Harmonic number (%)	50% magnetization	75% magnetization	100% magnetization
average	36.65	39.22	41.04
6 th	5.5	6.0	6.0
12 th	14.4	13.0	12.2
24 th	3	3.0	3.0
36 th	2.2	2	1.9
THD	16.05	15.10	14.48

3.8 CONCLUSION

This article develops a lumped magnetic circuit in a slot-less 6-pole series hybrid variable flux machine based on the existing magnetic circuit model available in the literature. The open circuit air gap flux density is calculated using the developed lumped magnetic circuit with 100%, 75% and 50% magnetization levels of the AlNiCo9 magnet. The results show that there is an insignificant difference between FEA and analytical results. The error between FEA and analytical air gap flux density increases as the magnetization level decreases. The error is less than 4% with different magnetization levels of the AlNiCo9 magnet. Thus, the magnetic circuit model is validated. The cogging torque of the 36-slot 6-

pole series hybrid variable flux machine is calculated utilizing the air gap flux density and the relative air gap permeance function at 50% and 100% magnetization levels. The results show that the computed cogging torque follows the FEA results at each magnetization level and also validated by measurement. There is a deviation between the FEA and computed waveforms of the cogging torque at each magnetization level. The deviation in the cogging torque waveform increases with lower magnetization levels as the error in air gap flux density increases at lower level of magnetizations.

The effect of cogging torque on back EMF and output torque waveform at different magnetization levels are analyzed in detail. It can be concluded that cogging torque has major impact on the quality of back EMF and output torque waveform at each magnetization level.

This chapter focused on a hybrid variable flux machine using an Alnico magnet and rare earth magnet in series. The next chapter considers a rare earth magnet specially designed to align the magnet and reluctance torques.

Chapter 4

Cogging Torque Computation in an Asymmetrical Interior Permanent Magnet Machine Using Lumped Parameter Technique

4.1 INTRODUCTION

Electric motors for vehicle applications require wide speed range with higher torque density and efficiency [48]. Permanent magnet synchronous machines (PMSM) can operate with high torque density and efficiency compared with similar induction machines. But the price of the rare earth magnets is higher. Therefore, current research looks for electrical machine technology that avoids rare earth materials or achieve the similar desired performance with lower magnet volume.

This article develops the lumped magnetic circuit of a novel asymmetrical IPM machine where the magnet torque is aligned with reluctance torque to enhance the torque density with reduced magnet volume. A flux barrier is introduced so that the magnet and reluctance axes move from their conventional positions. The peak value of magnet torque is then aligned with peak value of the reluctance torque. Thus, higher torque density in the asymmetrical IPM machine was achieved with lower magnet volume [49].

One of the major problems of the asymmetrical IPM machine is higher cogging torque and torque ripple [19], [50], [51]. The higher cogging torque in the asymmetrical IPM machine can create acoustic noise and vibration [52]. Therefore, it is crucial to know the value of the cogging torque in the asymmetrical IPM machine. The cogging torque in the asymmetrical IPM machine occurs due to the magnetic attraction between the permanent magnets (PMs) and slotted stator at no load. This cogging torque can create torque ripple at rated load operation [18]. Therefore, learning and minimizing the value the cogging torque in the asymmetrical IPM machine is highly important.

The cogging torque in the asymmetrical IPM machine can be computed based on a Fourier series of the asymmetrical flux distribution in the air gap in an equivalent slot-less

PM machine and the relative air gap permeance function [13]. However, due to significant leakage flux and magnetic saturation in IPM machines, it is very difficult to directly employ analytical methods to predict the open-circuit air-gap field distribution. Although finite-element analysis (FEA) can precisely obtain the flux density distribution, it can create computational burden and still often used only for design validation. Therefore, a lumped magnetic circuit model usually can be a good trade between simplicity and accuracy [37] – [40], [53]-[55]. The asymmetrical flux distribution in the 36-slot 4-pole IPM machine can be computed using an equivalent lumped magnetic circuit model derived based on the FEA results [41].

Lumped magnetic circuits are particularly applicable for IPM machines due to extremely saturated rotor bridges and intricate rotor configurations. The rotor bridges could be modeled as constant flux leakage sources with preset values [54], [55] or nonlinear permeance elements using iterative process [18], [38], [53]. Although the assumption in [39], [40] might be incorrect since the saturation level of the rotor iron bridge could be changed under different loading conditions, it was reasonably acceptable for estimation as it could result in significant simplification.

Hence, this paper presents improved lumped magnetic circuit models for analytically predicting the open-circuit air-gap flux density distributions in a 36-slot 4-pole asymmetrical IPM machine. Based on the analysis of flux lines obtained by FEA, simplified lumped magnetic circuits are obtained and Kirchhoff's law is used for deriving the analytical expressions of the leakage fluxes [41]. A simplified lumped magnetic circuit model based on flux distribution in the FEA is derived and necessary equations are found out to compute the open circuit air gap flux density.

Cogging torque derivation of an asymmetrical IPM machine is not available in the literature. Therefore, cogging torque of the asymmetrical 36-slot 4-pole IMP machine is derived based on the available information of cogging torque available in the literature [11], [56]-[58]. Finally, the cogging torque in the asymmetrical IPM machine is computed using the open circuit air gap flux density in an equivalent slot-less machine and unit relative air gap permeance function. The computed cogging torque is compared to the FEA results.

4.2 CHARACTERISTICS OF THE IPM MACHINE

The torque components of the inset PMSM in Fig. 4.1 were illustrated using the frozen permeability method [49], [60]. The asymmetrical IPM machine was simulated at full load at different current angles to obtain the total torque. Then, the permanent magnet was replaced by air and torque was achieved using the frozen permeability method. This torque is called reluctance torque. Finally, the reluctance torque was subtracted from the full load torque to obtain the magnet torque. This was clearly observed in Fig. 4.1 that magnet torque was aligned with the reluctance torque by creating asymmetrical barriers and thus the total torque of the machine was enhanced with a reduction of 30% magnet volume compared to surface PMSM with similar rating [49].

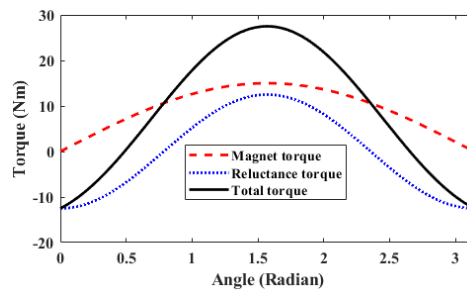


Fig. 4.1. Characteristics of the asymmetrical IPM machine [2].

4.3 LUMPED MAGNETIC CIRCUIT

The greatest common divisor of number of slot (36) and pole (4) of the asymmetrical IPM machine is 4. Therefore, a two-dimensional (2-D) section of 90° of the asymmetrical IPM machine is chosen to analyze the flux distribution in FEA. A 2-D section of the IPM machine with simulated flux lines is shown in Fig. 4.2. The necessary dimensions of the asymmetrical IPM machine are mentioned in Fig. 4.3 to develop the lumped magnetic circuit model.

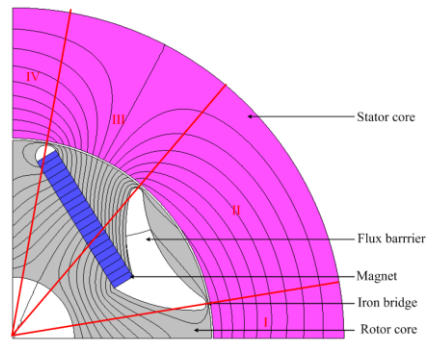


Fig. 4.2. 4-pole IPM including flux lines.

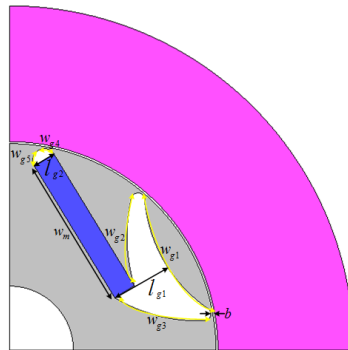


Fig. 4.3. Necessary dimensions to develop lumped model.

The pole pitch of the 4-pole asymmetric IPM machine is 90° . The 2-D section of the 4-pole asymmetrical IPM is divided into 4 regions to develop the simplified lumped magnetic circuit model. The span of the regions is taken into account counterclockwise. The region I is from 0° to 10° where the magnitude of the flux is almost negligible as shown in Fig. 4.2. The flux in the asymmetrical IPM machine in region II ($10^\circ - 50^\circ$) is lower than compared to

region III due to the presence of asymmetrical flux barrier which enhances the torque density in the asymmetrical IPM machine by aligning the peak magnet torque with the peak of reluctance torque at the same torque angle. The flux in the IPM machine mainly flows in the region III (50° - 80°). The magnitude of flux is again negligible in region IV (80° - 90°). There are three iron bridges as well in the 4-pole IPM machine. The bridge I is in series with bridge II. The leakage fluxed in bridge I is the same as in bridge 2 as they are in series. The leakage fluxes through air ϕ_{ml} and the corresponding leakage reluctances is R_{ml} . The magnet leakage reluctance is ϕ_{mo} and the corresponding leakage reluctance R_{mo} .

$$\phi_{mb1} = \phi_{mb2} = B_{sat}A_b \quad (4.1) \quad A_b = bL \quad (4.2)$$

$$\phi_{mb3} = B_{sat}A_b \quad (4.3) \quad \phi_r = B_r A_m = B_r w_m L \quad (4.4)$$

$$R_{g1} = \frac{g}{\mu_o A_g} \quad (4.5) \quad R_{g2} = \frac{l_{g1}+g}{\mu_o w_g L} \quad (4.6)$$

$$R_{ml} = \frac{l_{g2}}{\mu_o \frac{w_{g4}+w_{g5}}{2} L} \quad (4.7) \quad R_{mo} = \frac{h_m}{\mu_o \mu_r A_m} = \frac{l_{g2}}{\mu_o \mu_r w_m L} \quad (4.8)$$

$$w_{g3} = w_{g4} = \frac{\pi l_{g2}}{4} \quad (4.9) \quad w_g = (w_{g1} + w_{g2} + w_{g3})/2 \quad (4.10)$$

$$A_{g1} = \frac{1}{3} \frac{2\pi(R_i - g/2)}{N_p} L \quad (4.11) \quad A_{g2} = \frac{4}{9} \frac{2\pi(R_i - g/2)}{N_p} L \quad (4.12)$$

Where μ_r is the relative permeability of the PM. The rotor and stator core consist of M36G29 laminated steel. The B-H characteristics of the laminated steel is provided in Fig. 4.4. The saturated flux density is obtained from the available non-linear B-H characteristics of the laminated steel. The non-linear B-H characteristics of the laminated M36G29 is provided in Fig. 4.4. Here, b is the thickness of each iron bridge. L is the effective stack length of the 4-pole asymmetric IPM machine. w_g can be calculated as provided by (4.10).

The magnet flux can be calculated by multiplying the residual magnetic flux density (B_r) with the surface magnet area (A_m). The air gap area can be calculated by (4.11) which is needed to calculate the air gap reluctance R_{g1} .

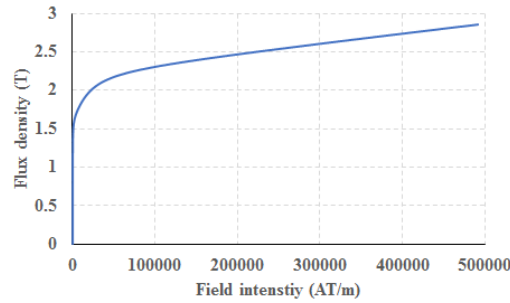


Fig. 4.4. B-H characteristics of M36G29 steel.

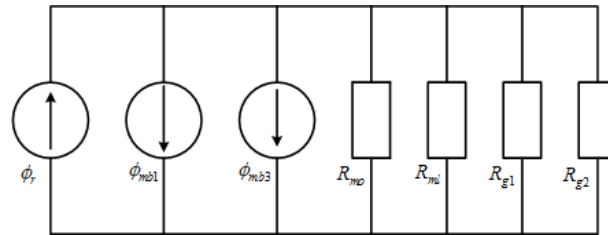


Fig.4.5. Lumped magnetic model of the asymmetrical IPM machine.

The lumped magnetic circuit can be derived as in Fig. 4.5 above. The necessary dimensions and parameters to calculate the magnetic quantities are shown in table 4.1.

Table 4.1. Necessary Dimensions and Parameters

B_r (T)	1.39 T
μ_r	1.0
g (mm)	0.5
b (mm)	0.5
l_{g1} (mm)	15.97
l_{g2} (mm)	6.00
R_i (mm)	54.5
N_p	4
w_{g1} (mm)	37.2
w_{g2} (mm)	24.03
w_{g3} (mm)	25.72

The air gap flux density is calculated using the lumped magnetic circuit developed in Fig. 4.5. The air gap flux density in region II and III are computed using the lumped magnetic

circuit in Fig. 4.5. The air flux density can be computed using (4.13) and (4.14). Equations (4.13) and (4.14) are derived from the lumped magnetic circuit model in Fig. 4.5. Thus, the air gap flux density can be computed using the developed lumped magnetic circuit model in Fig. 4.5. The computed air gap flux density in region II and III are compared to the FEA results in Fig. 4.6. The error between the computed air gap flux density and FEA in region II and III is mentioned in table 4.2. The comparison shows that computed air gap flux density follows the FEA results. Thus, the lumped magnetic circuit model is validated.

$$\phi_{g1} = \frac{\frac{\phi_r - \phi_{mb1} - \phi_{mb3}}{R_{g1}}}{\frac{1}{R_{g1}} + \frac{1}{R_{g2}} + \frac{1}{R_{ml}} + \frac{1}{R_{mo}}} \quad (13) \quad \phi_{g2} = \frac{\frac{\phi_r - \phi_{mb1} - \phi_{mb3}}{R_{g2}}}{\frac{1}{R_{g1}} + \frac{1}{R_{g2}} + \frac{1}{R_{ml}} + \frac{1}{R_{mo}}} \quad (14)$$

$$B_{g1} = \frac{\phi_{g1}}{A_{g1}} \quad (15) \quad B_{g2} = \frac{\phi_{g2}}{A_{g2}} \quad (16)$$

Table 4.2: Comparison between FEA and Analytical

Region	B_g (T) (FEA)	B_g (T) (Analytical)	Error (%)
II	0.0594	0.06	1.01
III	0.9696	0.9788	0.95

The percentage error between FEA and analytical is acceptable. The percentage error is higher in region II compared with region III as the magnitude of flux density is lower in region II compared to region III due to the presence of the asymmetrical flux barrier to enhance the torque density.

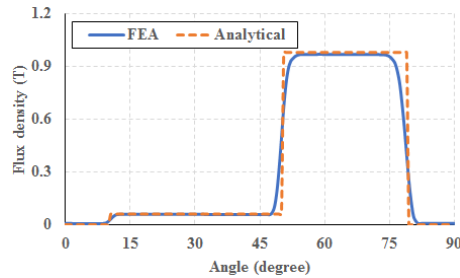


Fig. 4.6. Comparison of air gap flux density.

4.4 DERIVATION OF COGGING TORQUE

The asymmetrical IPM machine is designed such that peak magnet torque is aligned with peak reluctance torque to enhance the torque density. But the asymmetrical IPM machine is prone to higher cogging torque as it is a full pitched machine. Cogging torque occurs due to the magnetic attraction between the PMs and slotted stator at no load. Cogging torque does not contribute to the net effective torque causing torque pulsations. Cogging torque also causes acoustic noise and vibration. Therefore, computing the magnitude of the cogging torque in the asymmetrical IPM machine is very crucial.

The derivation of cogging torque with symmetrical PM and slot distribution is available in the existing literature. The derivations of the cogging torque with asymmetrical PMs are not available in the existing literature. This work tries to derive cogging torque in the asymmetrical 4-pole IPM machine based on energy variation method in the air gap. Therefore, the cogging torque can be expressed as [10], [56]

$$T_{cog}(\alpha) = -\frac{dW(\alpha)}{d\alpha} \quad (4.17)$$

Where $W(\alpha)$ is magnetic energy in the machine and function of the position angle (α) of the rotor. The magnetic energy can be expressed as,

$$W(\alpha) = \frac{1}{2\mu} \int B^2 dV \quad (4.18)$$

Where B is flux density in the various parts of the asymmetrical IPM machine and μ is the corresponding permeability. But the energy variation in the rotor and stator core, PM is negligible compared to the energy variation in the air gap. This is well known [41] that the air gap field distribution can be predicted from the product of air gap relative permeance and air gap flux density in an equivalent slot-less machine i.e.

$$B = G(\theta)B(\theta, \alpha) \quad (4.19)$$

Where $G(\theta)$ is the air gap relative permeance function and $B(\theta, \alpha)$ is the flux distribution in an equivalent slot-less asymmetrical IPM machine. Therefore, energy in the air gap can be rewritten as

$$W(\alpha) = \frac{L}{4\mu_o} (R_2^2 - R_1^2) \int_0^{2\pi} G^2(\theta) B^2(\theta, \alpha) \quad (4.20)$$

where μ_o is the permeability of air, R_2 is the outer radius of air gap, R_1 is the inner radius of air gap, θ is the angle along the circumference. Now, the number of the stator slots is N_S , and the period of $G^2(\theta)$ is $2\pi/N_S$. $G^2(\theta)$ in a symmetrically slot distributed machine can be expressed in the interval $[-\pi/N_S, \pi/N_S]$ as

$$G^2(\theta) = \sum_{k=1}^{\infty} G_{akN_S} \cos(kN_S\theta) \quad (4.21)$$

Where G_{akN_S} is the Fourier series coefficient. Similarly, the number poles in an IPM machine is N_P , asymmetrical flux distribution can be expressed in the interval $[-\pi/N_P, \pi/N_P]$ as,

$$B^2(\theta, \alpha) = \sum_{m=1}^{\infty} B_{amN_P} \cos(mN_P\theta) + B_{bmN_P} \sin(mN_P\theta) \quad (4.22)$$

Where B_{amN_P} and B_{bmN_P} are the Fourier series coefficients. The total energy in the air gap exists if the components satisfy $kN_S = mN_P$, the energy in the air gap is not zero. Therefore, letting, $kN_S = mN_P = nN_L$ where N_L is least common multiple of the number of slots (N_S) and number of poles (N_P)

$$N_L = LCM(N_S, N_P) \quad (4.23)$$

Therefore, cogging torque with asymmetrical flux distribution can be derived as follows

$$\begin{aligned}
T_{cog}(\alpha) &= \frac{\pi L N_L}{4\mu_0} (R_2^2 - R_1^2) \sum_{n=1}^{\infty} n G_{anN_L} B_{anN_L} \sin(nN_L \alpha) \\
&+ \sum_{n=1}^{\infty} n G_{anN_L} B_{bnN_L} \cos(nN_L \alpha) \quad (4.24)
\end{aligned}$$

4.5 FOURIER COEFFICIENTS

In this section, the Fourier coefficients in (4.24) are derived based on air gap flux density in an equivalent slot-less machine and unit relative air gap permeance function. The leakage flux of the PM-pole is neglected, and ideal air gap flux density is taken into account to compute the Fourier coefficients with asymmetrical flux distribution in the IPM machine. The slots are symmetrically distributed and accordingly Fourier coefficient of relative air gap function is derived.

4.5.A Determination of G_{anNL}

A slot is shown in Fig. 4.7 and the corresponding relative air gap permeance function is shown in Fig. 4.8. The relative air gap permeance function is utilized to compute the cogging torque of the 36-slot 4-pole asymmetrical IPM machine.

The Fourier coefficient of the relative air gap permeance function in (4.24) for the asymmetrically distributed PM machine with PM-pole on a rotor is obtained as follows.

$$\begin{aligned}
G_{anN_L} &= \frac{N_S}{\pi} \left(\int_{-\frac{\pi}{N_S}}^{-\frac{b}{N_S}} \cos(nN_L \theta) + \int_{\frac{\pi}{N_S}}^{\frac{b}{N_S}} \cos(nN_L \theta) \right) \\
&= -\frac{2N_S}{\pi n N_L} \sin\left(\frac{nN_L b}{2}\right) \quad (4.25)
\end{aligned}$$

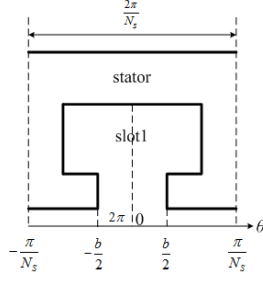


Fig. 4.7. A simplest slot.

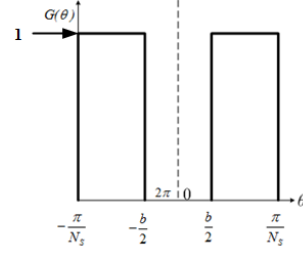


Fig. 4.8. Relative air gap permeance function.

4.5.B Determination of B_{anNL} and B_{bnNL}

The flux density in the air gap is asymmetrically distributed as shown in Fig. 4.6. Ideal flux distribution is considered to find the Fourier coefficients and leakage flux component is neglected in Fig. 4.9. Therefore, flux density component has both sine and cosine coefficients when it is expanded using Fourier series due to the asymmetrical distribution of the air gap flux density. The ideal asymmetrical flux distribution is shown in Fig. 4.9. The cosine Fourier coefficient can be calculated as follows.

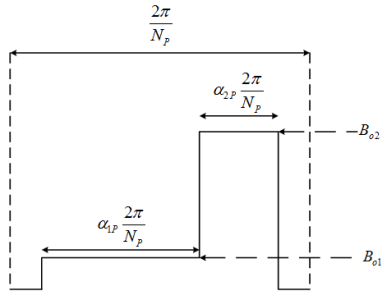


Fig. 4.9. Ideal flux distribution.

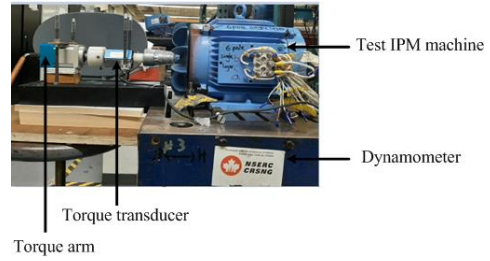


Fig. 4.10. Hardware setup.

$$B_{anNL} = \frac{N_P}{2\pi n N_L} \left(B_{o1}^2 \sin \left(n N_L \alpha_{1P} \frac{\pi}{N_P} \right) + B_{o2}^2 \sin \left(n N_L \alpha_{2P} \frac{\pi}{N_P} \right) \right) \quad (26)$$

$$B_{bnNL} = -\frac{N_P}{2\pi n N_L} \left(B_{o1}^2 \cos \left(n N_L \alpha_{1P} \frac{\pi}{N_P} \right) + B_{o2}^2 \cos \left(n N_L \alpha_{2P} \frac{\pi}{N_P} \right) \right) \quad (27)$$

Thus, the Fourier coefficients are found out by (4.25) – (4.27) and substituted into (4.24) to find the cogging torque of the 4-pole IPM machine with asymmetrical flux distribution.

4.6 COMPUTATION OF COGGING TORQUE

This section describes the hardware setup for the cogging torque measurement. The hardware setup consists of a torque arm, torque transducer, the test asymmetrical IPM machine and dynamometer. The model number of the torque transducer is T8-5-1A1. The interface torque transducer has a torque capability of 5 Nm with 5 V DC output voltages. The accuracy of the torque transducer is 0.25%. The torque transducer is connected to a personal computer to collect the measured cogging torque values. Cogging torque of the asymmetrical IPM machine is computed and compared to the FEA and experimental results. Cogging torque of the asymmetrical IPM machine is measured by rotating the shaft with the torque arm shown in Fig. 4.10.

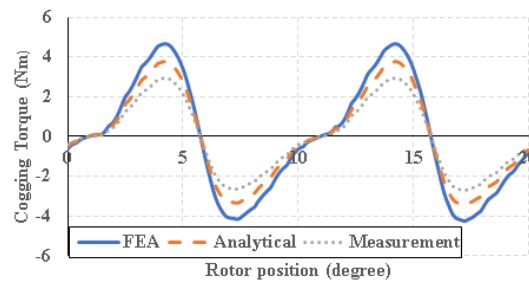


Fig. 4.11. Cogging torque.

Thus, cogging torque is derived in an asymmetrical IPM machine based on energy method using a Fourier series of flux density in an equivalent slot-less machine and relative air gap permeance function. The energy variation in the air gap occurs at a common frequency of the flux density distribution and relative air gap permeance function. The common frequency is the least common multiple of number of slots and poles and also the period of cogging torque. Higher value of the least common multiple indicates higher frequency of

cogging torque. Usually, the least common multiple is lower for the 36-slot 4-pole asymmetrical IPM machine, and the value is 36. Therefore, cogging torque of the asymmetrical IPM machine has a higher magnitude and a period of 10° as shown in Fig. 4.11.

4.7 CONCLUSION

The air gap flux distribution of the 4-pole asymmetrical IPM machine is calculated using lumped magnetic circuit model based on FEA flux distribution. The comparison between analytical and FEA shows that the computed air gap flux density agrees with the FEA results. The asymmetrical IPM has higher value of cogging torque. Therefore, calculating the value of cogging torque is important. The cogging torque in the 4-pole asymmetrical IPM machine is computed based on energy method using the Fourier series of flux density in an equivalent slot-less machine and relative air gap permeance function. The computed cogging torque follows the FEA results and is validated by measurement.

This chapter considered a special design of a PM machine to align the magnet and reluctance torques. The next chapter considers an axial field design with soft magnetic composite materials.

Chapter 5

Design of an Axial Flux Machine Using Soft Magnetic Composites

5.1 Sizing of Axial Flux Machine:

Design and sizing of a dual stator single rotor (DSSR) axial flux permanent magnet (AFPM) machine is discussed briefly in this section. This AFPM machine consists of two stator and one rotor between them. The rotor consists of PMs on the surface of rotor core both sides. The major dimensions of the DSSR AFPM machine are shown in Fig. 5.1, and they are calculated using the equations mentioned later in this section.

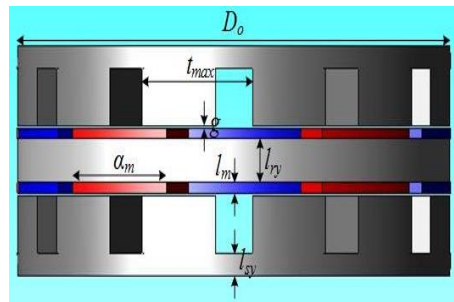


Fig. 5.1. Major dimensions of the DSSR AFPM machine; D_o = Outer diameter, t_{max} = Maximum slot pitch, g = Length of air gap, α_m = Span of one PM pole, l_m = Length of PM, l_{ry} = length of rotor yoke, l_{sy} = Length of stator yoke.

The stator outer diameter is calculated by using the following equation

$$D_o = \sqrt[3]{\frac{\varepsilon P_o}{\pi^2 K_D K_{w1} n_s B_{mg} A_m \eta \cos \phi}} \quad (5.1)$$

where ε is the ratio of generated back EMF to terminal voltage, P_o is rated output power, K_{w1} is fundamental winding factor, n_s is rotational speed in revolutions per second, B_{mg} is magnetic loading, A_m is electrical loading, η is efficiency and $\cos \phi$ is power factor of DSSR AFPM machine. Inner diameter is calculated by dividing the outer diameter by $\sqrt{3}$ to obtain the maximum torque theoretically.

Number of turns per phase per stator is calculated by the equation given below

$$N_1 = \frac{\varepsilon \frac{V_{ph}}{2}}{\pi \sqrt{2} f k_{w1} \phi_f} \quad (5.2)$$

where V_{ph} is phase voltage, N_1 is number of turns per stator per phase, f is fundamental frequency and ϕ_f is flux per pole.

Parallel slots are used to accommodate the copper winding in the stator of the AFPM machine. The design of stator slot depends on maximum flux density (B_{tmax}) in the narrowest part of stator.

$$B_{tmax} = \frac{B_{mg} \times t_{min}}{C_{min}} \quad (5.3)$$

where t_{min} is the minimum stator slot pitch and C_{min} is the narrowest tooth width in stator of AFPM machine. C_{min} is designed depending on the maximum flux density allowed in the narrowest part of stator tooth by equation (5.3)

The length of permanent magnet is obtained with the help of equation (5.4). The effect of sot opening is included by considering the carter coefficient in the equation (5.4).

$$l_m = \frac{\mu_{rrec} \times B_{mg} \times g \times K_c}{B_{ro} - B_{mg}} \quad (5.4)$$

where μ_{rrec} is relative recoil PM permeability, K_c is carter factor, B_{ro} residual flux density of PM.

The length of stator and rotor yoke are obtained by using the following two equations.

$$l_{sy} = \frac{\alpha_M B_{mg} \pi D_o}{4 p B_{sy} K_{st}} \quad (5.5)$$

$$l_{ry} = \frac{\alpha_M B_{mg} \pi D_o}{4 p B_{ry} K_{st}} \quad (5.6)$$

where α_M is PM span, B_{sy} is the maximum flux density at stator yoke, B_{ry} is the maximum flux density at rotor yoke, K_{st} represents stack length of rotor and stator yoke. K_{st} is considered 1 in the design process of AFPM machine as no laminated sheet is used as core material. Soft magnetic composite (SMC) material and iron core are used as core material in the stator and rotor respectively.

5.2 Simulation Results:

Table 5.1: SPECIFICATIONS OF THE 12 SLOT 14 POLE DSSR AFPM MACHINE

Output power	15 kW
Rated voltage	375 Volt
Rated speed	1500 rpm
Rated current	50.2 Amp
Pole number	14
Slot Number	12
Axial length	100 mm
Stator core material	Somaloy
Air gap	1 mm
PM material	NdFe
PM remanence	1.2 T
PM thickness	4.5 mm

In a two-stator one-rotor axial-flux surface-rotor machine, the rotor is either located between two slotted stators or two slot-less stators, whereas PMs are located on the surface of the rotor disc. Fig 5.2 shows the 3-D diagram of the 12-slot 14-pole 15 kW slotted DSSR AFPM machine [61]. Fig. 5.3 shows a quarter model which allows the simulation

with reduced computational burden. This figure is a 3-D configuration of the motor with concentrated winding. The advantage of DSSR AFPM machine is that the machine experiences zero attractive force along the axial length of the machine.

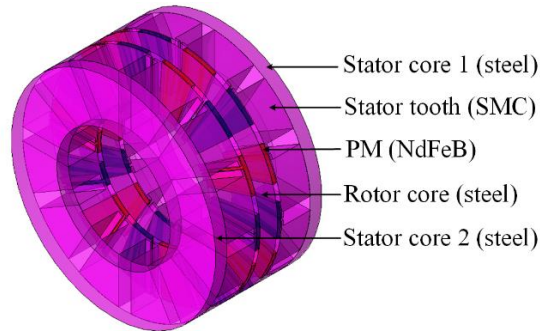


Fig 5.2. Full model of the 12-slot 14-pole 15 kW DSSR AFPM Machine.

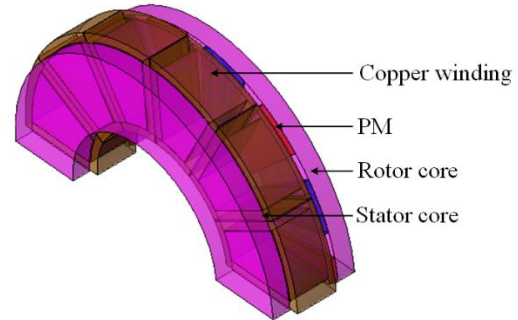


Fig 5.3. Quarter model of the DSSR AFPM machine.

The stator tooth consists of soft magnetic composite (SMC) material. The SMC materials are effective when the stator core is subjected to 3-D flux path. Therefore, it is important to investigate the performance of the axial flux machine with different soft magnetic composite materials. Material A has lower conductivity (70 S/m), material B has medium conductivity (600 S/m) and Material C higher conductivity (6000 S/m).

The 12 slot 14 pole dual stator single rotor is susceptible to no load attraction between slotted stator and PMs on the rotor. This attraction between the slotted stator and PMs is called cogging torque. Cogging torque with three materials are almost identical. The least common multiple of the number of slots and poles is 84. Therefore, Cogging torque has a period of 4.3° .

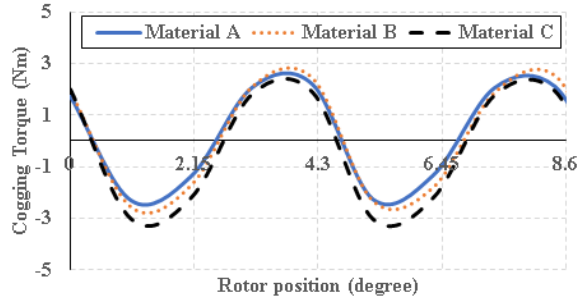


Fig. 5.4. Cogging torque of the DSSR AFPM machine with materials A, B, C.

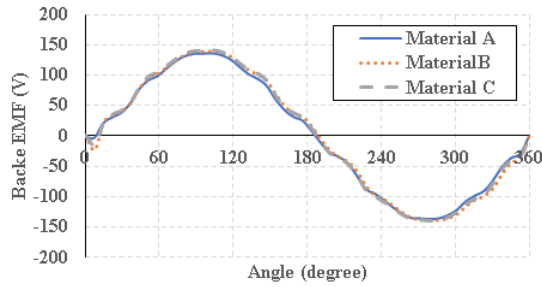


Fig. 5.5. Back EMF of the DSSR AFPM machine with materials A, B, C.

The back EMF of the DSSR AFPM machine is simulated with three different materials A, B, C in Fig. 5.5. The torque at rated current of the DSSR AFPM machine with three different materials is shown in Fig. 5.6.

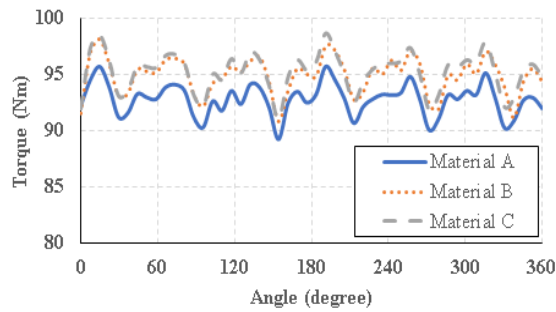


Fig. 5.6 Torque of the DSSR AFPM machine with materials A, B, C at rated current 50.2.

Table 5.2 shows a comparison of the 15 kW DSSR AFPM machine with three different SMC materials. The comparison shows that the performance of the 15 kW DSSR AFPM machine is

best with material B compared to material A and C. The loss comparison of the three materials is shown in table 5.2 and Fig. 5.7. The efficiency of the 15 kW AFPM machine in Fig. 5.8 is higher with material B compared to material A and C.

Table 5.2: DETAIL OF THE 12 SLOT 14 POLE AFPM MACHINE

	Material A	Material B	Material C
Materials			
Stator core	SMC Somaloy_110i_1P	SMC Somaloy_700HR_1P	SMC Somaloy_1000_5P
Rotor core	Steel M3629G	Steel M3629G	Steel M3629G
Conductor	Copper	Copper	Copper
Permanent magnet	NdFeB (1.2 T)	NdFeB (1.2 T)	NdFeB (1.2 T)
Machine parameter			
Number of slot and poles	12 slot and 14 poles		
Phase resistance (Ω)	0.025	0.025	0.025
Phase current, rms (A)	50.2	50.2	50.2
Base speed (rpm)	1500	1500	1500
Torque (Nm)	92.7	94.9	95.2
Loss parameter			
Conductor loss (W)	189.0	189.0	189.0
Magnet loss (W)	287.4	288.3	248.2
Hysteresis loss (W)	455.2	342.2	239.9
Eddy current loss (W)	7.2	56.9	496.3
Total iron loss (W)	462.4	399.1	736.2
Total loss (W)	954.9	876.4	1178.7
Efficiency (%)	94.0	94.5	92.7

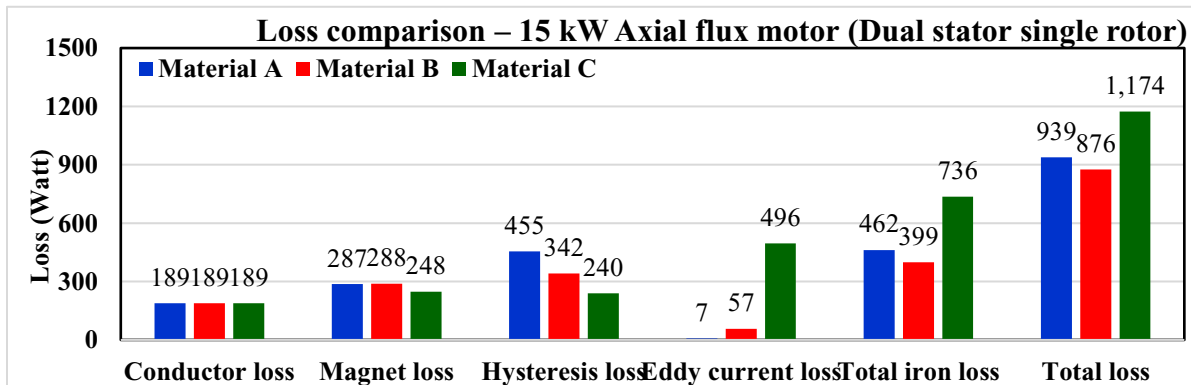


Fig. 5.7 Loss comparison of the 15 kW DSSR AFPM machine with A, B, C materials.

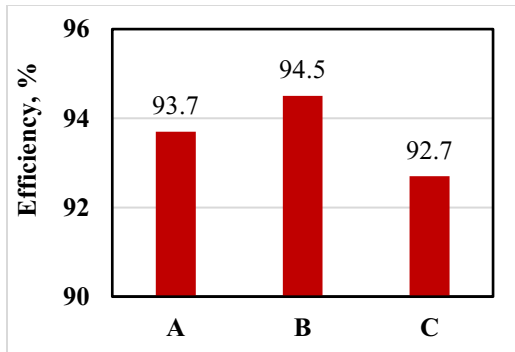


Fig 5.8. Efficiency comparison with 3 different materials

5.3 CONCLUSIONS

A 15 kW dual stator single rotor axial flux machine is designed with three different soft magnetic composite materials (SMC) of Somaloy. Material A has lower conductivity (70 S/m), material B has medium conductivity (600 S/m) and Material C higher conductivity (6000 S/m). The cogging torque based on materials A and B are similar while C has slightly higher cogging torque. However, the Somaloy material B with medium conductivity provides higher efficiency and is therefore the preferred choice.

The conclusions and future work are presented in chapter 6.

Chapter 6

CONCLUSIONS AND FUTURE WORK

The conclusions from chapter 2 to chapter 5 are drawn in chapter 6.

6.1 Chapter 2

This work reduces the cogging torque and hence the torque ripple in a 27 slot 6 pole VF IPMSM by step skewing the PMs. The cogging torque of the VF IPMSM is shown with different magnetization levels. The magnitude of the cogging torque increases with higher magnetization level. The cogging torque reduction is higher for optimum skewing angle with a 5-step skewed PM-pole than a 3-step skewed PM-pole at 100% magnetization. The FEA results show that skewing notably reduces the slot harmonics in the back EMF.

Torque ripple reduction is higher with a 5-step skewed PM-pole compared to a 3-step skewed PM-pole at each level of magnetization. The torque ripple is reduced by 6.4% at 100% magnetization, 7.6% at 75% magnetization and 8.9% at 50% magnetization with a 5-step skewed PM-pole. Therefore, the torque ripple reduction is higher at lower levels of magnetization. The average torque reduces with lower magnetization levels. Therefore, torque ripple increases with lower magnetization levels. The FEA and hardware results of the cogging torque for the unskewed rotor VF IPMSM are compared at 100% magnetization level. There is a rotor eccentricity in the VF IPMSM at 100% magnetization level and this can be the cause of the difference between measured and FEA results.

The unskewed PM-pole is demagnetized by applying a current pulse. The magnetic flux density of each step of the 3-step PM-pole can be brought close to zero with a current pulse for a skewing angle of $20/3^0$ compared to a skewing angle of $40/3^0$. Therefore, a skewing

angle of $20/3^0$ is preferable. There is no requirement of additional demagnetizing current for the step skewed PM-pole. The FEA results show that the unskewed as well as the 3-step skewed PM-pole is magnetized with a current pulse. This work resulted in the following publication, "D. Barman and P. Pillay, "Effect of Skewing in a Variable Flux Interior Permanent Magnet Synchronous Machine," in *IEEE Transactions on Industry Applications*, vol. 56, no. 6, pp. 6399-6410, Nov.-Dec. 2020.

The cogging torque of the VF IPMSM increases with higher magnetization level of Alnico magnets. The effect of skewing on cogging torque at different magnetization levels of Alnico magnet can be analyzed in future.

6.2 Chapter 3

This article develops a lumped magnetic circuit in a slot-less 6-pole series hybrid variable flux machine based on the existing magnetic circuit model available in the literature. The open circuit air gap flux density is calculated using the developed lumped magnetic circuit with 100%, 75% and 50% magnetization levels of the AlNiCo9 magnet. The results show that there is an insignificant difference between FEA and analytical results. The error between FEA and analytical air gap flux density increases as the magnetization level decreases. The error is less than 4% with different magnetization levels of the AlNiCo9 magnet. Thus, the magnetic circuit model is validated. The cogging torque of the 36-slot 6-pole series hybrid variable flux machine is calculated utilizing the air gap flux density and the relative air gap permeance function at 50% and 100% magnetization levels. The results show that the computed cogging torque follows the FEA results at each magnetization level and also validated by measurement. There is a deviation between the FEA and computed waveforms of the cogging torque at each magnetization level. The

deviation in the cogging torque waveform increases with lower magnetization levels as the error in air gap flux density increases at lower level of magnetizations.

The effect of cogging torque on back EMF and output torque waveform at different magnetization levels are analyzed in detail. It can be concluded that cogging torque has major impact on the quality of back EMF and output torque waveform at each magnetization level. This work resulted in the IEEE ECCE conference 2021 paper, “Cogging Torque Analysis in a Series Hybrid Variable flux machines using Lumped Magnetic Circuits” and will be submitted for IEEE Transactions in Industry Applications after presentation in ECCE.

Cogging torque of the series hybrid variable flux machine has been computed considering ideal air gap flux distribution at different magnetization levels of Alnico magnet. Based on the virtual permanent magnet (PM) concept the IPM can be considered as a surface PM machine and unit relative permeability, and then it is used for calculating the cogging torque with conventional techniques. Among the evaluation methods for cogging torque, the lateral force method, which is based on lateral force acting on stator teeth, can be selected to compute the cogging torque of the series hybrid variable flux machine.

6.3 Chapter 4

The air gap flux distribution of the 4-pole asymmetrical IPM machine is calculated using lumped magnetic circuit model based on FEA flux distribution. The comparison between analytical and FEA shows that the computed air gap flux density agrees with the FEA results. The asymmetrical IPM has higher value of cogging torque. Therefore,

calculating the value of cogging torque is important. The cogging torque in the 4-pole asymmetrical IPM machine is computed based on energy methods using the Fourier series of flux density in an equivalent slot-less machine and relative air gap permeance function. The computed cogging torque follows the FEA results and is validated by measurement. This work has resulted in the following paper submitted to the IEEE Transactions on Magnetics, "Cogging Torque Analysis in an Asymmetrical Interior Permanent Magnet synchronous machine using Lumped Parameter Technique".

The cogging torque of the IPM machine has been analyzed considering unit relative air gap permeance function. The effect of slot opening can be included to compute the cogging torque in future work.

6.4 Chapter 5

A 15 kW dual stator single rotor axial flux machine is designed with three different soft magnetic composite materials (SMC) of Somaloy. Material A has lower conductivity (70 S/m), material B has medium conductivity (600 S/m) and Material C higher conductivity (6000 S/m). The cogging torque based on materials A and B are similar while C has slightly higher cogging torque. However, the Somaloy material B with medium conductivity provides higher efficiency and is therefore the preferred choice. This work has resulted in the IEEE ECCE conference 2021 paper, "Selection of Soft Magnet Composite Material for Electrical Machines using 3D FEA Simulations".

Cogging torque of the axial flux machine depends on the shape of magnets. Cogging torque of the dual stator single rotor axial flux machine can be analyzed to observe the effect of magnet shapes on cogging torque.

REFERENCES

- [1] A. M. Aljehaimi and P. Pillay, "Operating Envelopes of the Variable-Flux Machine With Positive Reluctance Torque," in *IEEE Transactions on Transportation Electrification*, vol. 4, no. 3, pp. 707-719, Sept. 2018.
- [2] M. Ibrahim, L. Masisi and P. Pillay, "Design of Variable-Flux Permanent-Magnet Machines Using Alnico Magnets," in *IEEE Transactions on Industry Applications*, vol. 51, no. 6, pp. 4482-4491, Nov.-Dec. 2015.
- [3] A. Sun, J. Li, R. Qu, J. Chen, and H. Lu, "Rotor design considerations for a variable-flux flux-intensifying interior permanent magnet machine with improved torque quality and reduced magnetization current," in Proc. IEEE Energy Convers. Congr. Expo. (ECCE), Sep. 2015, pp. 784–790.
- [4] V. Ostovic, "Memory motors," *IEEE Ind. Appl. Mag.*, vol. 9, no. 1, pp. 52–61, Jan./Feb. 2003.
- [5] N. Limsuwan, T. Kato, K. Akatsu and R. D. Lorenz, "Design and Evaluation of a Variable-Flux Flux-Intensifying Interior Permanent-Magnet Machine," in *IEEE Transactions on Industry Applications*, vol. 50, no. 2, pp. 1015-1024, March-April 2014..
- [6] K. Sakai, K. Yuki, Y. Hashiba, N. Takahashi, and K. Yasui, "Principle of the variable-magnetic-force memory motor," in Proc. Int. Conf. Electr. Mach. Syst., Nov. 2009, pp. 1–6.
- [7] A. Athavale, K. Sasaki, B. S. Gagas, T. Kato, and R. D. Lorenz, "Variable flux permanent magnet synchronous machine (VF-PMSM) design methodologies to meet electric vehicle traction requirements with reduced losses," *IEEE Trans. Ind. Appl.*, vol. 53, no. 5, pp. 4318–4326, Sep./Oct. 2017.
- [8] H. Hua, Z. Q. Zhu, A. Pride, R. Deodhar, and T. Sasaki, "A novel variable flux memory machine with series hybrid magnets," in Proc. IEEE Energy Convers. Congr. Expo. (ECCE), Sep. 2016, pp. 1–8.
- [9] A. Takbash, M. Ibrahim and P. Pillay, "Design Optimization of a Spoke-Type Variable Flux Motor Using AlNiCo for Electrified Transportation," in *IEEE Transactions on Transportation Electrification*, vol. 4, no. 2, pp. 536-547, June 2018.

- [10] N. Bianchi and S. Bolognani, "Design techniques for reducing the cogging torque in surface-mounted PM motors," in *IEEE Transactions on Industry Applications*, vol. 38, no. 5, pp. 1259-1265, Sept.-Oct. 2002.
- [11] L. Zhu, S. Z. Jiang, Z. Q. Zhu and C. C. Chan, "Analytical Methods for Minimizing Cogging Torque in Permanent-Magnet Machines," in *IEEE Transactions on Magnetics*, vol. 45, no. 4, pp. 2023-2031, April 2009.
- [12] X. Ge, Z. Q. Zhu, G. Kemp, D. Moule and C. Williams, "Optimal Step-Skew Methods for Cogging Torque Reduction Accounting for Three-Dimensional Effect of Interior Permanent Magnet Machines," in *IEEE Transactions on Energy Conversion*, vol. 32, no. 1, pp. 222-232, March 2017.
- [13] D. Barman, S. Sengupta and T. K. Bhattacharya, "Cogging torque reduction in surface mounted permanent magnet synchronous machine," *2016 IEEE International Conference on Power Electronics, Drives and Energy Systems (PEDES)*, Trivandrum, 2016, pp. 1-5.
- [14] D. Barman and P. Pillay, "Effect of Skewing in a Variable Flux Interior Permanent Magnet Synchronous Machine," *2018 IEEE International Conference on Power Electronics, Drives and Energy Systems (PEDES)*, Chennai, India, 2018, pp. 1-6.
- [15] J. A. Güemes, A. M. Iraolagoitia, J. I. Del Hoyo and P. Fernández, "Torque Analysis in Permanent-Magnet Synchronous Motors: A Comparative Study," in *IEEE Transactions on Energy Conversion*, vol. 26, no. 1, pp. 55-63, March 2011.
- [16] M. Barcaro and N. Bianchi, "Torque ripple reduction in fractional-slot Interior PM machines optimizing the flux-barrier geometries," *2012 XXth International Conference on Electrical Machines*, Marseille, 2012, pp. 1496-1502.
- [17] W. Q. Chu and Z. Q. Zhu, "Reduction of On-Load Torque Ripples in Permanent Magnet Synchronous Machines by Improved Skewing," in *IEEE Transactions on Magnetics*, vol. 49, no. 7, pp. 3822-3825, July 2013.
- [18] D. Wang, X. Wang and S. Jung, "Cogging Torque Minimization and Torque Ripple Suppression in Surface-Mounted Permanent Magnet Synchronous Machines Using Different Magnet Widths," in *IEEE Transactions on Magnetics*, vol. 49, no. 5, pp. 2295-2298, May 2013.

- [19] W. Ren, Q. Xu, Q. Li and L. Zhou, "Reduction of Cogging Torque and Torque Ripple in Interior PM Machines With Asymmetrical V-Type Rotor Design," in *IEEE Transactions on Magnetics*, vol. 52, no. 7, pp. 1-5, July 2016, Art no. 8104105.
- [20] A. Takbash, M. Ibrahim and P. Pillay, "Torque ripple reduction of a variable flux motor," *2016 IEEE Energy Conversion Congress and Exposition (ECCE)*, Milwaukee, WI, 2016, pp. 1-7.
- [21] R. Thike and P. Pillay, "Characterization of a Variable Flux Machine for Transportation Using a Vector-Controlled Drive," in *IEEE Transactions on Transportation Electrification*, vol. 4, no. 2, pp. 494-505, June 2018.
- [22] B. S. Gagas, K. Sasaki, T. Fukushige, A. Athavale, T. Kato and R. D. Lorenz, "Analysis of Magnetizing Trajectories for Variable Flux PM Synchronous Machines Considering Voltage, High-Speed Capability, Torque Ripple, and Time Duration," in *IEEE Transactions on Industry Applications*, vol. 52, no. 5, pp. 4029-4038, Sept.-Oct. 2016.
- [23] C. Desai and P. Pillay, "Back EMF, Torque–Angle, and Core Loss Characterization of a Variable-Flux Permanent-Magnet Machine," in *IEEE Transactions on Transportation Electrification*, vol. 5, no. 2, pp. 371-384, June 2019.
- [24] C. Desai and P. Pillay, "Torque and core loss characterization of a variable-flux permanent-magnet machine," *2016 IEEE Energy Conversion Congress and Exposition (ECCE)*, Milwaukee, WI, 2016, pp. 1-6.
- [25] A. Takbash and P. Pillay, "Magnetization and Demagnetization Energy Estimation and Torque Characterization of a Variable-Flux Machine," in *IEEE Transactions on Energy Conversion*, vol. 33, no. 4, pp. 1837-1845, Dec. 2018.
- [26] M. Ibrahim, L. Masisi and P. Pillay, "Design of Variable Flux Permanent-Magnet Machine for Reduced Inverter Rating," in *IEEE Transactions on Industry Applications*, vol. 51, no. 5, pp. 3666-3674, Sept.-Oct. 2015.
- [27] R. Imamura and R. D. Lorenz, "Analytical Methods for Spatially Varying MMF Vectors to Adjust Back-EMF Harmonics and Torque Ripple in Variable Magnetization Pattern Machines," *2018 IEEE Energy Conversion Congress and Exposition (ECCE)*, Portland, OR, 2018, pp. 4979-4986.

- [28] M. A. Khan, I. Husain, M. R. Islam and J. T. Klass, "Design of Experiments to Address Manufacturing Tolerances and Process Variations Influencing Cogging Torque and Back EMF in the Mass Production of the Permanent-Magnet Synchronous Motors," in *IEEE Transactions on Industry Applications*, vol. 50, no. 1, pp. 346-355, Jan.-Feb. 2014.
- [29] T. M. Jahns G. Kliman T. Neumann "Interior permanent-magnet synchronous motors for adjustable-speed drives" *IEEE Trans. Ind. Appl.* vol. IA-22 no. 4 pp. 738-747 Jul./Aug. 1986.
- [30] H. Liu, H. Lin, F. Shuhua and X. Huang, "Investigation of influence of permanent magnet shape on field-control parameters of variable flux memory motor with FEM," *Proceedings of the Automation Congress Conference*, Sept. 2008.
- [31] Z. Changqing, W. Xiuhe and W. Bei, "Study of a novel permanent magnet synchronous motor with composite-rotor," *Proceedings of the International Conference on Electrical Machines and Systems (ICEMS)*, pp.1044-1047, Oct. 2010.
- [32] G. Zhou, T. Miyazaki, et al. "Development of variable magnetic flux motor suitable for electric vehicle," *Proceedings of the International Power Electronics Conference (IPEC)*, pp. 2171-2174, Jun. 2010.
- [33] M. Ibrahim and P. Pillay, "Design of Hybrid Variable Flux Motors for Enhanced Wide-Speed Performance," *2019 IEEE Energy Conversion Congress and Exposition (ECCE)*, Baltimore, MD, USA, 2019, pp. 6046-6053.
- [34] L. J. Wu, Z. Q. Zhu, D. A. Staton, M. Popescu and D. Hawkins, "Comparison of Analytical Models of Cogging Torque in Surface-Mounted PM Machines," in *IEEE Transactions on Industrial Electronics*, vol. 59, no. 6, pp. 2414-2425, June 2012.
- [35] Z. Q. Zhu, S. Ruangsinchaiwanich and D. Howe, "Synthesis of cogging-torque waveform from analysis of a single stator slot," in *IEEE Transactions on Industry Applications*, vol. 42, no. 3, pp. 650-657, May-June 2006.
- [36] Z. Q. Zhu and D. Howe, "Analytical prediction of the cogging torque in radial-field permanent magnet brushless motors," in *IEEE Transactions on Magnetics*, vol. 28, no. 2, pp. 1371-1374, March 1992.

- [37] Wen-Bin Tsai and Ting-Yu Chang, "Analysis of flux leakage in a brushless permanent-magnet motor with embedded magnets," in *IEEE Transactions on Magnetics*, vol. 35, no. 1, pp. 543-547, Jan. 1999.
- [38] M. Rahman, T. Little and G. Slemon, "Analytical models for interior-type permanent magnet synchronous motors," in *IEEE Transactions on Magnetics*, vol. 21, no. 5, pp. 1741-1743, September 1985.
- [39] Chang-Chou Hwang and Y. H. Cho, "Effects of leakage flux on magnetic fields of interior permanent magnet synchronous motors," in *IEEE Transactions on Magnetics*, vol. 37, no. 4, pp. 3021-3024, July 2001.
- [40] E. C. Lovelace, T. M. Jahns and J. H. Lang, "A saturating lumped parameter model for an interior PM synchronous machine," *IEEE International Electric Machines and Drives Conference. IEMDC'99. Proceedings (Cat. No.99EX272)*, Seattle, WA, USA, 1999, pp. 553-555.
- [41] L. Zhu, S. Z. Jiang, Z. Q. Zhu and C. C. Chan, "Analytical Modeling of Open-Circuit Air-Gap Field Distributions in Multisegment and Multilayer Interior Permanent-Magnet Machines," in *IEEE Transactions on Magnetics*, vol. 45, no. 8, pp. 3121-3130, Aug. 2009.
- [42] J. H. Seo and H. S. Choi, "Cogging Torque Calculation for IPM Having Single Layer Based on Magnetic Circuit Model," in *IEEE Transactions on Magnetics*, vol. 50, no. 10, pp. 1-4, Oct. 2014.
- [43] J. H. Seo and H. S. Choi, "Analytical Modeling for Calculating Cogging Torque in Interior Permanent Magnet Machine With Multi Flux-Barriers," in *IEEE Transactions on Applied Superconductivity*, vol. 24, no. 3, pp. 1-4, June 2014.
- [44] Sang-Moon Hwang, Jae-Boo Eom, Geun-Bae Hwang, Weui-Bong Jeong and Yoong-Ho Jung, "Cogging torque and acoustic noise reduction in permanent magnet motors by teeth pairing," in *IEEE Transactions on Magnetics*, vol. 36, no. 5, pp. 3144-3146, Sept 2000.
- [45] Sang-Moon Hwang, Jae-Boo Eom, Yoong-Ho Jung, Deug-Woo Lee and Beom-Soo Kang, "Various design techniques to reduce cogging torque by controlling energy variation in permanent magnet motors," in *IEEE Transactions on Magnetics*, vol. 37, no. 4, pp. 2806-2809, July 2001.

- [46] R. Lateb, N. Takorabet and F. Meibody-Tabar, "Effect of magnet segmentation on the cogging torque in surface-mounted permanent-magnet motors," in *IEEE Transactions on Magnetics*, vol. 42, no. 3, pp. 442-445, March 2006.
- [47] J. Wanjiku, M. A. Khan, P. S. Barendse and P. Pillay, "Influence of Slot Openings and Tooth Profile on Cogging Torque in Axial-Flux PM Machines," in *IEEE Transactions on Industrial Electronics*, vol. 62, no. 12, pp. 7578-7589, Dec. 2015.
- [48] T. J. E. Miller, *Brushless Permanent-Magnet and Reluctance Motor Drives*. New York: Oxford University Press, 1989.
- [49] M. Ibrahim and P. Pillay, "Aligning the Reluctance and Magnet Torque in Permanent Magnet Synchronous Motors for Improved Performance," *2018 IEEE Energy Conversion Congress and Exposition (ECCE)*, 2018, pp. 2286-2291.
- [50] D. Wu and Z. Q. Zhu, "Design Tradeoff Between Cogging Torque and Torque Ripple in Fractional Slot Surface-Mounted Permanent Magnet Machines," in *IEEE Transactions on Magnetics*, vol. 51, no. 11, pp. 1-4, Nov. 2015.
- [51] J. Gao, G. Wang, X. Liu, W. Zhang, S. Huang and H. Li, "Cogging Torque Reduction by Elementary-Cogging-Unit Shift for Permanent Magnet Machines," in *IEEE Transactions on Magnetics*, vol. 53, no. 11, pp. 1-5, Nov. 2017, Art no. 8208705.
- [52] Z. Q. Zhu, Y. Liu and D. Howe, "Minimizing the Influence of Cogging Torque on Vibration of PM Brushless Machines by Direct Torque Control," in *IEEE Transactions on Magnetics*, vol. 42, no. 10, pp. 3512-3514, Oct. 2006.
- [53] C. Mi, M. Filippa, W. Liu, and R. Q. Ma, "Analytical method for predicting the air-gap flux of interior-type permanent-magnet machines," *IEEE Trans. Magn.*, vol. 40, no. 1, pp. 50-58, Jan. 2004.
- [54] S. H. Han, T. M. Jahns, and W. L. Soong, "A magnetic circuit model for an IPM synchronous machine incorporating moving airgap and crosscoupled saturation effects," in *Proc. IEEE Int. Electric Machines and Drives Conf. (IEMDC)*, May 3-5, 2007, pp. 21-26.
- [55] N. Matsui, M. Nakamura, and T. Kosaka, "Instantaneous torque analysis of hybrid stepping motor," *IEEE Trans. Ind. Appl.*, vol. 32, no. 5, pp. 1176-1182, 1996.

- [56] Z. Q. Zhu and D. Howe, "Influence of design parameters on cogging torque in permanent magnet motors," *IEEE Trans. Energy Convers.*, vol. 15, no. 4, pp. 407–412, 2000.
- [57] B. Ackermann, J. H. H. Janssen, R. Sottek, and R. I. van Steen, "New technique for reducing cogging torque in a class of brushless DC motors," *Proc. Inst. Elect. Eng. B*, vol. 139, no. 4, pp. 315–320, 1992.
- [58] D. C. Hanselman, "Effect of skew, pole count and slot count on brushless motor radial force, cogging torque and back EMF," *Proc. Inst. Elect. Eng.*, vol. 144, no. 5, pp. 325–330, 1997.
- [59] Touzhu Li and G. Slemon, "Reduction of cogging torque in permanent magnet motors," in *IEEE Transactions on Magnetics*, vol. 24, no. 6, pp. 2901-2903, Nov. 1988.
- [60] M. Popescu, D. M. Ionel, T. J. E. Miller, S. J. Dellinger, and M. I. McGilp, "Improved finite element computations of torque in brushless permanent magnet motors," *IEE Proceeding on Electric Power Applications*, vol. 152, no. 2, pp. 271–276, Mar. 2005.
- [61] D. Nguyen, K. Tseng, S. Zhang and H. T. Nguyen, "A Novel Axial Flux Permanent-Magnet Machine for Flywheel Energy Storage System: Design and Analysis," in *IEEE Transactions on Industrial Electronics*, vol. 58, no. 9, pp. 3784-3794, Sept. 2011.
- [62] A. Hemeida, M. Taha, A. A. -. Abdallah, H. Vansompel, L. Dupré and P. Sergeant, "Applicability of Fractional Slot Axial Flux Permanent Magnet Synchronous Machines in the Field Weakening Region," in *IEEE Transactions on Energy Conversion*, vol. 32, no. 1, pp. 111-121, March 2017,
- [63] Jacek F. Gieras, Rong-Jie Wang, Marteen J. Kamper, "Axial Flux Permanent Magnet Brushless Machines" 2nd edition, Springer publications.